Fragile polyQ assemblies cause Golgipathy in Huntington's disease

Lixiang Ma[1*#], Xinyu Chen[1*], Yang Liu[1*], Lijun Dai[2*], Fangzhou Ye[1*], Weiqi Yang[1*], Hada Buhe[1], Jixin Ma[1], Chenyun Song[1], Li Li[3], Dandan Fan[2], Fanxun Chen[4], Haoman Chen[4], Jianwei, Shuai[4], Jianzhong Su[2#], Hexige Saiyin[4#]

1. Department of Anatomy, Histology & Embryology, School of Basic Medical Science, Fudan University, Shanghai 200032, People's Republic of China

2. Department of Anesthesiology, Huashan Hospital, Fudan University, Shanghai, China.

3. Oujiang Laboratory (Zhejiang Lab for Regenerative Medicine, Vision and Brain Health), Wenzhou Medical University, Zhejiang 325001, China

4. Wenzhou Institute, University of Chinese Academy of Sciences, Wenzhou, 325000, China4

5. School of Life Sciences, Fudan University, Shanghai, 200438, People's Republic of China

#Correspondence should be addressed to saiyin@fudan.edu.cn or lxma@fudan.edu.cn, sujz@wmu.edu.cn

*The authors equally contributed to this work.

Abstract

Huntingtin (HTT) is a naturally aggregating protein that causes Huntington's disease (HD) when its polyglutamine (polyQ) tract exceeds 38 repeats. Despite its importance, the biology of HTT aggregates remains poorly defined. Utilizing high-resolution imaging of HD family-derived cells, we have redefined polyQ assemblies—formerly viewed as pathogenic aggregates—as dynamic structures resembling knitted-fabric patches. These assemblies encircle the Golgi apparatus, integrating ribbons and stacks to form a functional polyQ assembly-Golgi complex and attaching clathrin vesicles. Mechanistically, we show that the fragmentation of polyQ assemblies is dynamically coupled with mitotic Golgi fragmentation and that treatment with the ARF inhibitor Brefeldin A splits and fragments the complex. The presence of mutant HTT (mHTT) 'crisps' these assemblies and complexes, altering their response to nutrient deprivation and autophagy enhancers but not to antisense oligonucleotide (ASO) therapy. The polyQ assembly in HD cells also reduces the scaffolding capacity of the Golgi apparatus, clathrin vesicles, and ARF1, impairing Golgi functions. Our results demonstrate that mHTT disrupts the homeostatic dynamics of the polyQ assembly-Golgi complex, inducing a 'Golgipathy' by crippling Golgi structure and function.

Introduction

Huntington's disease (HD) is a devastating neurodegenerative disorder characterized by irreversible neuronal loss in the striatum, resulting in profound motor dysfunction and cognitive decline(Kernich, 2002; Saudou and Humbert, 2016; Walker, 2007a). The condition is driven by the expansion of a polyglutamine (polyQ) tract within the Huntingtin (HTT) protein, rendering it highly prone to aggregation (Gutekunst et al., 1999). Notably, HTT aggregates exhibit significant instability following chemical fixation (Ferrante et al., 1997), a histological challenge that can lead to the misinterpretation of polyQ biology and pathophysiology if standardized protocols are not strictly applied.

While polyQ aggregate formation and the presence of intranuclear inclusion bodies are traditionally considered pathological hallmarks of HD (DiFiglia et al., 1997; Gutekunst et al., 1999), their precise role remains controversial. Emerging evidence suggests a paradox: some studies indicate that aggregate formation may actually increase single-neuron survival (Arrasate et al., 2004), exerting a protective rather than toxic effect (Kim et al., 1999; Saudou et al., 1998). Conversely, soluble monomeric HTT and its transition into oligomeric species—which precede fibril and inclusion body formation—are the primary drivers of cellular toxicity (Hatters et al., 2013; Jimenez-Sanchez et al., 2017; Lajoie and Snapp, 2010; Legleiter et al., 2010; Mukai et al., 2005; Poirier et al., 2002; Takahashi et al., 2008). These observations suggest that mature HTT aggregates may possess critical biological functions rather than being purely pathogenic.

HTT is a stiff protein composed of multiple α-helical and PolyQ (Dougan et al., 2009; Guo et al., 2018; Saudou and Humbert, 2016; Sivaramakrishnan et al., 2008; Tabrizi et al., 2020). Expanded polyQ (>35) and short polyQ form a rigid fibril (Bauerlein et al., 2017; Dougan et al., 2009; Isas et al., 2017; Scherzinger et al., 1999); however, expanded polyQ fibrils have been reported

to physically disrupt organelle membranes, such as the endoplasmic reticulum (ER), and alter membrane dynamics (Bauerlein et al., 2017). Functionally, HTT acts as a versatile scaffold involved in a wide array of cellular processes, including vesicular transport, autophagy, gene transcription, and embryonic development (Saudou and Humbert, 2016). HTTs are an essential protein in embryonic development (Dragatsis et al., 1998; Duyao et al., 1995; Zeitlin et al., 1995). The presence of mutant HTT (mHTT) precipitates widespread cellular dysfunction, ranging from early transcriptional dysregulation and synaptic impairment to mitochondrial distress and disruption of the nuclear pore complex (Costa et al., 2010; del Toro et al., 2009; DiFiglia et al., 1997; Grima et al., 2017; Kim et al., 2010; Mehta et al., 2018; Milnerwood et al., 2006; Saudou and Humbert, 2016; Shirasaki et al., 2012). mHTT induces extrasynaptic excitotoxicity(Milnerwood et al., 2010), higher levels of brain inflammation(Lee et al., 2020; Silvestroni et al., 2009), abnormal fetal brain development(Barnat et al., 2020), and aging(Machiela and Southwell, 2020). HAP40 stabilizes HTT(Guo et al., 2018; Harding et al., 2021). HTT interacts with and activates dynamin, a protein that catalyzes membrane fission (Caviston et al., 2007; Caviston et al., 2011; Morlot and Roux, 2013), microtubule motors, and actin-associated adaptors to support cellular vesicle transport, including autophagy, endosomes, and lysosomes (Caviston et al., 2011; Olenick and Holzbaur, 2019).

Using HD family-derived cells and super-resolution scanning, we revealed a knitted-fabric-like network formed by HTT polyQ that encircles flat Golgi stacks/cisternae and dynamically couples with both mitotic and stress-related Golgi fragmentation. We demonstrate that while normal polyQ assemblies support the structural integrity of the Golgi, pathogenic mHTT "crisps" these assemblies, destabilizing the complex and impairing Golgi activities. Our findings reveal that the polyQ assembly-Golgi complex is a highly organized functional unit, the disruption of which represents a central mechanism of

mHTT-induced toxicity.

Results

Characterization of endogenous polyQ aggregate structure

We identified an HD family in the Mongolian population of West China. 24 persons have identifiable syndromes, including an adult-onset, abnormal gait, uncontrolled arm, leg, and head movements, and psychiatric abnormalities; some patients with severe syndromes showed mania and pica **(Table S1).** The self-reported symptoms appeared at ages 24 to 50; patients died from 35 to 56 **(Table S1)**. Genetic testing revealed that the patients in this family harbor 44 to 59 CAG repeats in *HTT* **(Fig. 1A, B; Table S1)**, compared with 18-19 CAG repeats in healthy individuals. Consistent with HD, the lengths of CAG repeats define the disease onset age, symptom severity, and death age **(Fig. 1C; Table S1).**

To assess polyQ status in fibroblasts from this HD family, we stained them with the 3B5H10 antibody, a polyQ antibody that equally recognizes both HTT and mHT polyQ (Owens et al., 2015). We observed that the polyQ of fibroblasts, including patients and healthy siblings, exhibits well-organized assemblies that resemble knitted fabrics formed by two paralleled spindles that interfused at a regular interval, structurally resembling an assembly of multiple rings (**Fig. 2A)**. Contrary to other observation(Tousley et al., 2019), phalloidin counterstaining showed that the polyQ assembly did not regularly parallel actin filaments and randomly interact with action filaments **(Fig. 2A)**. 3D rendered tomography showed that the polyQ assembly in fibroblasts interacts with the nuclear membrane **(Fig. 2A)**. Notably, the size of polyQ assemblies in HD is similar to that in healthy fibroblasts (HD: n=4; healthy: n=4) **(Fig. 2B, C)**. Mitochondria did not preferentially enrich in the polyQ assembly site: some of them were present in the polyQ assembly network's space, others were not **(Fig. 2D).** The polyQ assemblies were fragmented in mitotic cells **(Fig. 2E)**. Strikingly, the polyQ assemblies fragmented after 4% PFA fixation: the immediate staining after fixation is the only way to visualize

an intact polyQ assembly **(Fig. 2F)**. These findings indicate that polyQ assemblies are a unique, dynamic polyQ assembly with a specific structure in cells.

PolyQ assemblies of HD patients and healthy individuals differentially respond to stress and drugs

Antisense oligonucleotides (ASOs) reduce the transcription of *HTT(Kordasiewicz et al., 2012)*. To test how the polyQ assemblies in fibroblasts respond to ASO, we treated the HD family fibroblasts with ASO (20 and 40 μM) and found that the ASO equally reduced the polyQ assemblies in healthy and HD fibroblasts without affecting the structure of polyQ assembly **(Fig. 3A-C).** Autophagy-enhancing agents were reported to reduce mHTT(Martin et al., 2015). We also treated HD fibroblasts with onjisaponin F (5, 10, 20, and 40 μM), an active component of the polygala tenuifolia(Nagai et al., 2001). Onjisaponin F reduced polyQ assemblies in HD fibroblasts, but not those in healthy fibroblasts, in a dose-dependent manner, without fragmenting polyQ assemblies **(Fig. 3D, E)**. To see how the polyQ assemblies respond to energy deprivation, we cultured the fibroblasts from 4 patients with HD (CAG: 48, 49, 55, and 59) and 2 healthy siblings in a low-glucose medium. We fixed cells at 24, 48, and 72 h and evaluated the polyQ assemblies. Under glucose deprivation, the polyQ assemblies in HD fibroblasts are diminished and fragmented over time. In contrast, polyQ assemblies in healthy fibroblasts are stable, and the smaller polyQ fragments in healthy cells are decreased **(Fig. 3F-H)**. After culturing in the low-glucose medium for 72 h, we switched to a high-glucose medium. After culturing for an additional 48 h, we observed that the polyQ assemblies in HD fibroblasts had been restored **(Fig. 3F-H)**. Together, the presence of pathogenic polyQ shifts the response of polyQ assemblies to energy deprivation and to an autophagy-enhancing treatment in fibroblasts.

PolyQ assemblies circle the Golgi apparatus.

HTTs are present on the surface of the Golgi, and mHTT impairs Golgi trafficking (del Toro et al., 2009; del Toro et al., 2006; DiFiglia et al., 1995). To our knowledge, the appearance of polyQ assemblies resembles Golgi ribbons. GM130, a Golgi marker, and 3B5H10 coimmunostaining revealed that polyQ assemblies circle flat Golgi ribbon/stacks; the flat Golgi stack stands between the internal space of two parallel spindles of polyQ assemblies, and an isthmus-like hollow in Golgi appeared at where polyQ circled Golgi cisternae **(Fig. 4A)**, indicating the physical interactions of the Golgi apparatus with polyQ assemblies. The size of the Golgi apparatus in HD fibroblasts is smaller than that of healthy cells **(Fig. 4B).** Clathrin-coated vesicles sort on Golgi(Klumperman, 2011). Clathrin+ vesicles preferentially distributed along or conjugated with polyQ assemblies **(Fig. 4C),** and polyQ assemblies in HD fibroblasts attached fewer clathrin^{+} vesicles than polyQ assemblies in healthy fibroblasts **(Fig. 4D).** To localize the C-terminal of HTT in the polyQ assemblies, we stained the polyQ with a 3B5H10 antibody and the C-terminal with a C-terminal-specific antibody (LSB11011) and found that discontinuous C-terminal signals are present in the polyQ assemblies, and the C-terminal of HCC reside inside the assembly **(Fig. 4E).** We also noticed that some smaller polyQ assemblies which conjugate with abundant actin filiaments are present in the cytoplasm or ruffluring membrane of fibroblasts **(Fig.S1A-C)**. Huntingtin-associated protein 40 (HAP40), a protein coevolved with HTT, binds to all three domains of HTT and stabilizes HTT(Guo et al., 2018; Harding et al., 2021). HAP40 resided on the corner of the network in polyQ assemblies, polyQ assemblies in HD, and healthy cells attached the same amount of HAP40 **(Fig. 4F, G).**

The Golgi apparatus fragments during cell mitosis and reassembles after mitosis (Wei and Seemann, 2009). PolyQ assemblies and Golgi stack/ribbon fragment during prometaphase (28 cells from 6 samples) and anaphase (23 cells from 6 samples), and reassemble at the late telophase (22 cells from 6 samples), and the fragmented Golgi in the mitotic cells conjugate with polyQ

patches **(Fig. 4H).** Consistent with our previous reports(Liu et al., 2024), the polyQ assemblies in HD fibroblasts attached fewer ARF1, and Brefeldin A (BFA) treatments decouple polyQ assemblies from the Golgi apparatus in all fibroblasts **(Fig. 4I-M)**. ARF1, which conjugates to the Golgi after converting its GDP to GTP-ATP in a GTP-ATP-dependent manner(D'Souza-Schorey and Chavrier, 2006), couples polyQ assembly to the Golgi (Liu et al., 2024). Thus, it is rational to hypothesize that polyQ assembly in HD fibroblasts is sensitive to energy deprivation. To test this hypothesis, we also immunostained HD patient fibroblasts and their healthy siblings that had been starved for 48 h with antibodies against 3B5H10 and GM130. Consistent with the changes of polyQ assemblies of HD and healthy cells under stress, the Golgi ribbons of HD fibroblasts loosened and fragmented, and most polyQ fragments/patches attached by Golgi fragments in glucose deprivation **(Fig. S1F),** whereas the structure of Golgi ribbons is stable, and the small Golgi fragments are reduced in healthy fibroblasts after culturing in a low glucose medium for 48h **(Fig. S1F, G).** In addition, we observed that HD patient cells with higher CAG repeat counts (55) had more fragmented Golgi than those with lower CAG repeat counts (49) after 48 h of glucose deprivation **(Fig. S1H)**. The size of the Golgi in HD fibroblasts is reduced more quickly than that of its healthy siblings after 48 h glucose starvation **(Fig. S1I).** Together, our findings indicate that polyQ assemblies form a polyQ assembly-Golgi apparatus complex impaired by the presence of mHTT. To see *in vivo* Golgi dynamics in a living fibroblast, we continuously monitored fibroblasts (CAG: 49, 55, 19, and 19) stained by Golgi apparatus-selective dye after glucose starvation or H_2O_2 stimulation. The Golgi apparatus in HD patient fibroblasts is easier to fragment under glucose starvation than healthy fibroblasts **(Fig. 4N, O)**, whereas the Golgi apparatus in patients and healthy fibroblasts uniformly fragments under H_20_2 stimulation **(Fig. S1D, E).**

Impaired polyQ assembly in HD neurons is associated with deficient golgi function in cortical and striatal neurons

We generated iPSCs from the family fibroblasts and differentiated them into GABAergic projection neurons in 2D [Ma et al., 2012]. On day 90, long polyQ assemblies are present in striatal neuronal projections, and fragmented polyQ assemblies were deposited in the neuronal nucleus of an HD patient with CAG 59 **(Fig. 5A).** PolyQ almost completely occupied the nucleus of some HD striatal neurons around 100 days in all patient neurons (CAG 47-59), but PolyQ did not appear in the nucleus of healthy striatal neurons with over 90 days of culture **(Fig. 5A, B)**. DIC images revealed that an intact, observable, deeply invaginated gorge where polyQ assemblies reside or traverse appeared in neurons, and 3D tomographic rendering showed that polyQ spindles also created a gorge on the nuclear surface **(Fig. S2A)**, indicating that polyQ assemblies are an intact and rigid structure. In addition, the striatal neurons with polyQ nuclear accumulation showed a pale-stained nucleus, nuclear membranes pocked by polyQ, and nuclear fragmentations **(Fig. S2B-F).** The fragmentation of polyQ also existed in human fetal and child brain samples, but not in fresh human brain organoid samples **(Fig. S3A-C).** Despite the fragmentation of polyQ assemblies in brain tissues, the structure of polyQ assemblies and their interaction pattern with the nucleus are identical to those of the polyQ assemblies in human brain organoids **(Fig. S3B; Fig.5A, B).** The necrosis-dependent fragmentation of polyQ assemblies in brain organoids was common **(Fig. S3D)**. The proteomic data also showed that nuclear activities in the HD striatal organoids (hStrO), including chromatin and DNA complex assembly, protein-DNA complex, DNA packaging complex, and nucleosome binding, were impaired in hStrO cultured for more than 60 days **(Fig. S4A, B).**

We also characterized the relationship between polyQ assemblies and the Golgi in neurons of hStrO and cortical organoids (hCOs) **(Fig. S4A, C)** (Chen et al., 2022). PolyQ assemblies include a flat Golgi stacks in hCOs**,** and the surface of Golgi in HD neurons were irregular **(Fig. 5C)**. Multiple Golgi also resided in the polyQ assemblies of striatal neurons in hStrO, which traversed

through the nuclear surface **(Fig. 5D).** PolyQ assemblies in the HD striatal neurons conjugate fewer Golgi than polyQ assemblies in healthy striatal neurons of hStrO **(Fig. 5E).** Clathrin+ vesicles preferentially distributed along or conjugated to polyQ assemblies in the HD and healthy neurons **(Fig. 5F).** Consistent with the results of fibroblasts, polyQ assemblies in HD neurons of hStrO attached fewer clathrin+ vesicles and ARF1 than that of healthy polyQ assemblies **(Fig. 5F, G; Fig. S5A-C)**, and Golgi apparatus in HD neurons also attached fewer ARF1 puncta than that of healthy Golgi **(Fig. S5D-F).** In addition, *ARF1* transcription levels in HD hStrOs are uniformly lower than those of healthy hStrO (60 and 80 days) **Fig.S5G, H).** Striatal projection neurons have extremely long dendrites and axon(Lanciego et al., 2012). Extended polyQ assemblies in HD striatal neuronal projections in hStrO, which resemble human striatal neuronal polyQ assembly, attached fewer fragmented/small Golgi than healthy polyQ assemblies **(Fig. 5H-I);** small Golgi resided in the hole of rings or attached to the outer spines of long polyQ assemblies in hStrO neurons **(Fig. 5N).** Clathrin+ vesicles interact with the polyQ assemblies and mainly reside on the two sides of the assemblies in the neurons of hStrO **(Fig. 5O).**

To test the functional impact of deficient polyQ assemblies-Golgi complexes on HD neuronal activities, we performed HD-MEA recordings on 80-day hCOs. Control organoids exhibited robust, highly synchronized network bursts, resembling the coded activity patterns of developing human brains **(Fig. 5K).** In contrast, HD hCOs displayed erratic firing patterns **(Fig. 5K).** Quantitative analysis revealed a significant reduction in both spikes per burst and the inter-burst interval (IBI) in HD hCOs **(Fig. 5L)**. Notably, the elevated IBI CV in HD hCOs signifies a disruption in the periodicity and rhythmic regularity of spontaneous network-wide bursting. These findings demonstrate that polyQ assemblies-mediated pathologenesis disrupts the emergence of functional network oscillations and collective neuronal firing in cortical circuits**.**

Impaired Golgi function in HD striatal neurons

We performed single-cell RNA sequencing (scRNA-seq) analyses of human striatal organoids (hStrOs) derived from hESC-H9, hiPSC-8-12 (CAG 19), and HD hiPSC-7-2 (CAG 59) after 110 days of culture. Transcriptomic data of 38,716 single cells were obtained after quality control and filtering **(Fig. 6A)**. Uniform manifold approximation and projection (UMAP) clustering identified four clusters in hStrOs that expressed cell-type-specific markers, including progenitor (VIM, NES, HES1), neuron (SYT1, DCX, STMN2), astrocytes (S100β, GFAP), and oligodendrocytes (OLIG2, SOX10) **(Fig. 6B, C, and S6A)**. We further plotted the expression of brain region-specific markers in these clusters and found that both control and HD hStrOs are primarily composed of LGE progenitors and GABAergic neurons rather than cortical progenitors and glutaminergic neurons (Fig. S6C, D), consistent with our protocols for generating hStrOs(Chen et al., 2022). Based on the characteristics of Golgi in HD fibroblasts**,** we compared the transcriptomes of mature GABAergic neurons in the control and HD groups after sorting the GABAergic neuron population using GAD1 and GAD2, specific markers for mature GABAergic neurons **(Fig. S6D-F)**. In the GABAergic neurons, the DEGs of HD hStrO extensively overlapped with those of hiPSC-derived hStrO (CAG 19) and hESC-derived hStrO, both for up-regulated (321 genes) and down-regulated genes (550 genes) **(Fig. 6D)**. Up-regulated genes in GO terms are associated with nuclear activities, including ribonucleoprotein complex assembly, translational initiation, and regulation of translation, which might be related to the nuclear poking of polyQ assemblies or deposition of polyQ into the nucleus. Interestingly, the down-regulated genes in GABAergic neurons of HD hStrOs were notably enriched for GO terms associated with Golgi or Golgi-related functions, including Golgi vesicle transport, endoplasmic reticulum to Golgi vesicle−mediated transport, vesicle organization, endomembrane system organization, intracellular protein transport, protein localization to membrane translation **(Fig. 6E)**. The down-regulated genes in HD hStrOs belong to Golgi matrix proteins, including

GOLGA8A, a structurally similar protein of GM130 enriched in neurons, *GOLGA4*, and Golgi matrix-associated GTPs that include *RAB6, ARL1/4C*, and *ARF1/3/4.*

Onjisaponin F did not mitigate polyQ nuclear accumulation, nor did ASO treatment normalize HD neuronal firing rates

We selected iPSCs from two HD patients (CAG 59 and 49), one healthy sibling, and the H9 cell line, and differentiated them into striatal neurons in 2D to test the effects of onjisaponin F on striatal neurons. We exposed iPSC-derived GABAergic neurons to a single dose of 20 μM onjisaponin F for 24 h on days 42 and 60. After culturing for another 48 h, we fixed the striatal neurons, assessed polyQ changes, and found that onjisaponin F treatment on days 42 and 60 reduced polyQ assembly volume in HD striatal neurons but not in healthy neurons **(Fig. 7A-C)**. We treated induced HD and healthy striatal neurons with 3 doses of onjisaponin F for 24h on days 50, 60, and 70. The immunostaining at day 90 showed that 3 doses of onjisaponin (10 μM) decreased the cytoplasmic and total volume of polyQ assemblies in HD striatal neurons but did not reduce the nuclear deposition of polyQ; the immunostaining at day 110 revealed that 3 doses of onjisaponin (20 μM) did not change the volume of polyQ assembly in healthy striatal neurons **(Fig.7D-E).**

Given that ASOs have demonstrated efficacy in promoting mHTT degradation across experimental models(Kordasiewicz et al., 2012) and have reduced the polyQ assembly size in human fibroblasts. We utilized ASO as a benchmark to evaluate its therapeutic impact on the polyQ assembly-driven phenotypes in hCOs. Following treatment, we observed downward trends in both spikes per burst and the IBI **(Fig. 7F, G).** The IBI coefficient of variation (CV) also trended lower, suggesting a subtle shift toward improved firing patterns **(Fig. 7F, G).** However, these alterations failed to reach statistical significance across 10 days **(Fig. 7F, G)**. The analysis of polyQ, Golgi, and ARF1 by immunostaining revealed that ASO treatment reduced the size of

polyQ assemblies in HD-hCOs but did not alter the Golgi tomography and inclusion, Golgi/ARF1 conjugation to polyQ assemblies **(Fig. 7H-K; Fig. S7A-D)**. These findings demonstrate that, under the tested conditions, the ASO treatment was insufficient to achieve a significant functional recovery of the HD-hCO network dynamics and rescue the Golgipathy in HD-hCOs.

Discussion

Here, we redefine the biology and structure of HTT polyQ aggregates, previously characterized as pathogenic aggregates(Truant et al., 2008). Using cells from a large, isolated HD family and state-of-the-art scanning, we show the polyQ assemblies of HTTs are large, dynamic, and well-organized structural networks composed of two or more long, parallel, and interfused spindles that encircle the Golgi apparatus, bind clathrin vesicles, and form a polyQ assembly-Golgi complex, which is structurally and dynamically coupled. The presence of mHTT shifts the response of polyQ assembly to energy deprivation and to autophagy-enhancing drugs, and destabilizes the Golgi apparatus by impairing ARF recruitment, inducing a Golgipathy in HD patients.

The Golgi ribbon comprises up to 100 flat stacks, composed of 4-11 stapled cisternae, in which newly synthesized soluble cargo proteins and lipids are processed and sorted, linked by tubular bridges in mammalian cells (Klumperman, 2011; Liu et al., 2021). The Golgi matrix, a ribosome-free protein network surrounding the cisternae, supports the stack structure(Ravichandran et al., 2020). The spatiotemporal relationships of polyQ assemblies with the Golgi apparatus, clathrin-coated vesicles, and ARF1 indicate that rigid polyQ assemblies serve as a structural component of the Golgi matrix, providing a scaffold for the Golgi apparatus and Golgi activities, including shaping, assembly, and sorting. ARFIP2, which interacts or conjugates multiple guanine nucleotide exchange factors (GEFs), including ARF1, ARF3, ARF5, and ARF6 (Wu and Zhou, 2009), directly conjugates with HTTs (Peters et al., 2002). Thus, it is rational to hypothesize that the ARFIP2-ARF complex mediates the relationship between polyQ assembly and the Golgi apparatus. The decoupling of the polyQ assembly-Golgi complex by BFA, but not during mitotic Golgi fragmentation, supports that the ARFIP2-ARF1 complex mediates this assembly.

Golgipathy, including structural and functional abnormality, is common in neurodegenerative diseases (El Ghouzzi and Boncompain, 2022; Klumperman,

2011; Liu et al., 2021; Passemard et al., 2017). The correct Golgi positioning is critical for cellular polarization and differentiation (Yadav and Linstedt, 2011); The precise localization of the Golgi apparatus mediates the simple spindle-like cells to form the dentate granule cells (DGCs) (Rao et al., 2018); GM130 deletion causes neurodegeneration and ataxia (Liu et al., 2017). Pathogenic *GORASP1 and ARF3* variants cause a neurodevelopmental disorder with neurosensory, neuromuscular, and skeletal abnormalities via affecting the cell cycle and glycosylation (Fasano et al., 2022; Lebon et al., 2025; Sakamoto et al., 2021). Previously, we reported that polyQ assemblies in HD cortical neurons altered corticogenesis by impairing ARF1 recruitment to the Golgi apparatus in the neuroepithelium(Liu et al., 2024).

The striatal projection neurons, which contain a prominent long polyQ assembly and polyQ nuclear accumulation, are lost early in HD patients (Walker, 2007b). HTT is a rigid protein (Dougan et al., 2009; Guo et al., 2018; Saudou and Humbert, 2016; Sivaramakrishnan et al., 2008; Tabrizi et al., 2020). The conjugation of ARF1 to the Golgi consumes ATP(D'Souza-Schorey and Chavrier, 2006). The glucose metabolism in HD patients is stronger than that of a healthy individual (Tang et al., 2013). Based on the body's compensation mechanism, the deficient ARF1 conjugation to the Golgi apparatus in HD might contribute to increased brain metabolism. The polyQ assembly-Golgi apparatus complex in HD striatal neurons needs more ATP to stabilize and function. Onjisaponin F, a strong autophagy enhancer, preferentially reduces the polyQ assembly in HD fibroblasts and striatal projection neurons without changing the structure of polyQ assembly. However, it did not rescue nuclear polyQ deposition, a hallmark of HD pathology(DiFiglia et al., 1997). Based on the spatial relationship of polyQ assembly with the neuronal nucleus and the rigid nature of polyQ, it is rational to consider that the fragility of HTT assembly, rather than the size of polyQ assembly, might be the cause of nuclear accumulation in long-term cultured striatal neurons. A well-test ASO(Kordasiewicz et al., 2012) reduced the size of polyQ assemblies

in HD cells but did not correct aberrant neuronal firings in HD cortical neurons, indicating that the structure of polyQ assembly-Golgi complex in HD cells drives aberrant neuronal activity. However, the size of polyQ assemblies does not matter.

Our study reveals the structure of polyQ aggregates and their spatial-temporal relationship with the Golgi apparatus, and demonstrates that mHTT destabilizes the polyQ assembly-Golgi complexes, dismantles the recruitment of Golgi activity-related proteins, leading to Golgipathy in HD. Thus, improving Golgi function and stabilizing polyQ assembly in HD might represent another approach to treating HD.

The limitation of this study

While our study provides a new structural framework for Huntingtin biology, several limitations remain. First, the specific mHTT-to-wtHTT ratio likely influences the degree of functional deficiency in the polyQ-Golgi complex, yet the precise incorporation pattern of mHTT into the polyQ assemblies remains to be determined. Second, while we characterized the fragility of polyQ assemblies under stress in HD cells, it is unclear how this structural instability relates to the subsequent nuclear deposition of polyQ. Future studies utilizing super-resolution and longterm imaging in the living HD cells may be required to visualize the real-time assembly and transition of these complexes into nuclear inclusions.

Materials and methods

Ethics

The ethics of this HD work was approved (No. 28) by the Ethics Committee of the Institutes of Biomedical Sciences at Fudan University. All HD family members who participated in this study signed a written consent form translated into Mongolian and consent to enter this study and authorisation for publication has been obtained. Dr. Li Li collected the human brain samples. The ethics approval number was obtained from the Huashan Hospital Ethics Committee (KY2018-310.01).

Human fibroblast and blood sample collection

After obtaining consent, a surgeon collected skin samples from the upper arm using a Skin Punch (diameter, 0.3 x 0.3 cm). After collecting samples, a nurse and doctor visited the patients daily for 7 days to prevent inflammation. The tissues were harvested into a tube with culturing medium supplied with antibiotics. After being transported to a lab, tissues were moved to a Biosafety Cabinet, sliced into smaller fragments with surgical knives, and then attached to dishes with forceps and cultured in a small amount of medium. After fully attaching to dishes, the tissues were placed in sufficient medium and cultured continuously for several weeks to obtain sufficient fibroblasts.

Author contributions

HS and LM set up this study. HS and LM performed most of the experiments; HS analyzed the data and prepared the manuscripts; XC, WY, YL, BH, and JX performed image analysis and immunostaining. XC, LY, and LM constructed organoids.

Financial supports

This work was supported by the National Natural Science Foundation of China (grant no. 32370852 and U24A2014 to LM) and the National Key Research and Development Program of China (grant no. 2021YFA1101302 to LM)

Conflict of Interest

All authors claim that there are no conflicts of interest.

Reference

Arrasate, M., Mitra, S., Schweitzer, E.S., Segal, M.R., and Finkbeiner, S. (2004). Inclusion body formation reduces levels of mutant huntingtin and the risk of neuronal death. Nature *431*, 805-810.

Barnat, M., Capizzi, M., Aparicio, E., Boluda, S., Wennagel, D., Kacher, R., Kassem, R., Lenoir, S., Agasse, F., Braz, B.Y.*, et al.* (2020). Huntington's disease alters human neurodevelopment. Science *369*, 787-793.

Bauerlein, F.J.B., Saha, I., Mishra, A., Kalemanov, M., Martinez-Sanchez, A., Klein, R., Dudanova, I., Hipp, M.S., Hartl, F.U., Baumeister, W.*, et al.* (2017). In Situ Architecture and Cellular Interactions of PolyQ Inclusions. Cell *171*, 179-187 e110.

Caviston, J.P., Ross, J.L., Antony, S.M., Tokito, M., and Holzbaur, E.L. (2007). Huntingtin facilitates dynein/dynactin-mediated vesicle transport. Proc Natl Acad Sci U S A *104*, 10045-10050.

Caviston, J.P., Zajac, A.L., Tokito, M., and Holzbaur, E.L. (2011). Huntingtin coordinates the dynein-mediated dynamic positioning of endosomes and lysosomes. Mol Biol Cell *22*, 478-492.

Chen, X., Saiyin, H., Liu, Y., Wang, Y., Li, X., Ji, R., and Ma, L. (2022). Human striatal organoids derived from pluripotent stem cells recapitulate striatal development and compartments. Plos Biol *20*, e3001868.

Costa, V., Giacomello, M., Hudec, R., Lopreiato, R., Ermak, G., Lim, D., Malorni, W., Davies, K.J., Carafoli, E., and Scorrano, L. (2010). Mitochondrial fission and cristae disruption increase the response of cell models of Huntington's disease to apoptotic stimuli. EMBO Mol Med *2*, 490-503.

D'Souza-Schorey, C., and Chavrier, P. (2006). ARF proteins: roles in membrane traffic and beyond. Nat Rev Mol Cell Biol *7*, 347-358.

del Toro, D., Alberch, J., Lazaro-Dieguez, F., Martin-Ibanez, R., Xifro, X., Egea, G., and Canals, J.M. (2009). Mutant huntingtin impairs post-Golgi trafficking to lysosomes by delocalizing optineurin/Rab8 complex from the Golgi apparatus. Mol Biol Cell *20*, 1478-1492.

del Toro, D., Canals, J.M., Gines, S., Kojima, M., Egea, G., and Alberch, J. (2006). Mutant huntingtin impairs the post-Golgi trafficking of brain-derived neurotrophic factor but not its Val66Met polymorphism. J Neurosci *26*, 12748-12757.

DiFiglia, M., Sapp, E., Chase, K., Schwarz, C., Meloni, A., Young, C., Martin, E., Vonsattel, J.P., Carraway, R., Reeves, S.A.*, et al.* (1995). Huntingtin is a cytoplasmic protein associated with vesicles in human and rat brain neurons. Neuron *14*, 1075-1081.

DiFiglia, M., Sapp, E., Chase, K.O., Davies, S.W., Bates, G.P., Vonsattel, J.P., and Aronin, N. (1997). Aggregation of huntingtin in neuronal intranuclear inclusions and dystrophic neurites in brain. Science *277*, 1990-1993.

Dougan, L., Li, J., Badilla, C.L., Berne, B.J., and Fernandez, J.M. (2009). Single homopolypeptide chains collapse into mechanically rigid conformations. Proc Natl Acad Sci U S A *106*, 12605-12610.

Dragatsis, I., Efstratiadis, A., and Zeitlin, S. (1998). Mouse mutant embryos lacking huntingtin are rescued from lethality by wild-type extraembryonic tissues. Development *125*, 1529-1539.

Duyao, M.P., Auerbach, A.B., Ryan, A., Persichetti, F., Barnes, G.T., McNeil, S.M., Ge, P., Vonsattel, J.P., Gusella, J.F., Joyner, A.L.*, et al.* (1995). Inactivation of the mouse Huntington's disease gene homolog Hdh. Science *269*, 407-410.

El Ghouzzi, V., and Boncompain, G. (2022). Golgipathies reveal the critical role of the sorting machinery in brain and skeletal development. Nat Commun *13*, 7397.

Fasano, G., Muto, V., Radio, F.C., Venditti, M., Mosaddeghzadeh, N., Coppola, S., Paradisi, G., Zara, E., Bazgir, F., Ziegler, A.*, et al.* (2022). Dominant ARF3 variants disrupt Golgi integrity and cause a neurodevelopmental disorder recapitulated in zebrafish. Nat Commun *13*, 6841.
Ferrante, R.J., Gutekunst, C.A., Persichetti, F., McNeil, S.M., Kowall, N.W., Gusella, J.F., MacDonald, M.E., Beal, M.F., and Hersch, S.M. (1997). Heterogeneous topographic and cellular distribution of huntingtin expression in the normal human neostriatum. J Neurosci *17*, 3052-3063.
Grima, J.C., Daigle, J.G., Arbez, N., Cunningham, K.C., Zhang, K., Ochaba, J., Geater, C., Morozko, E., Stocksdale, J., Glatzer, J.C.*, et al.* (2017). Mutant Huntingtin Disrupts the Nuclear Pore Complex. Neuron *94*, 93-107 e106.
Guo, Q., Bin, H., Cheng, J., Seefelder, M., Engler, T., Pfeifer, G., Oeckl, P., Otto, M., Moser, F., Maurer, M.*, et al.* (2018). The cryo-electron microscopy structure of huntingtin. Nature *555*, 117-120.
Gutekunst, C.A., Li, S.H., Yi, H., Mulroy, J.S., Kuemmerle, S., Jones, R., Rye, D., Ferrante, R.J., Hersch, S.M., and Li, X.J. (1999). Nuclear and neuropil aggregates in Huntington's disease: relationship to neuropathology. J Neurosci *19*, 2522-2534.
Harding, R.J., Deme, J.C., Hevler, J.F., Tamara, S., Lemak, A., Cantle, J.P., Szewczyk, M.M., Begeja, N., Goss, S., Zuo, X.*, et al.* (2021). Huntingtin structure is orchestrated by HAP40 and shows a polyglutamine expansion-specific interaction with exon 1. Commun Biol *4*, 1374.
Hatters, D.M., Hannan, A.J., and Springer Science+Business Media (2013). Tandem repeats in genes, proteins, and disease : methods and protocols (New York: Humana Press).
Isas, J.M., Langen, A., Isas, M.C., Pandey, N.K., and Siemer, A.B. (2017). Formation and Structure of Wild Type Huntingtin Exon-1 Fibrils. Biochemistry-Us *56*, 3579-3586.
Jimenez-Sanchez, M., Licitra, F., Underwood, B.R., and Rubinsztein, D.C. (2017). Huntington's Disease: Mechanisms of Pathogenesis and Therapeutic Strategies. Cold Spring Harb Perspect Med *7*.
Kernich, C.A. (2002). Huntington's disease. Neurologist *8*, 207-208.
Kim, J., Moody, J.P., Edgerly, C.K., Bordiuk, O.L., Cormier, K., Smith, K., Beal, M.F., and Ferrante, R.J. (2010). Mitochondrial loss, dysfunction and altered dynamics in Huntington's disease. Hum Mol Genet *19*, 3919-3935.
Kim, M., Lee, H.S., LaForet, G., McIntyre, C., Martin, E.J., Chang, P., Kim, T.W., Williams, M., Reddy, P.H., Tagle, D.*, et al.* (1999). Mutant huntingtin expression in clonal striatal cells: dissociation of inclusion formation and neuronal survival by caspase inhibition. J Neurosci *19*, 964-973.
Klumperman, J. (2011). Architecture of the mammalian Golgi. Cold Spring Harb Perspect Biol *3*.
Kordasiewicz, H.B., Stanek, L.M., Wancewicz, E.V., Mazur, C., McAlonis, M.M., Pytel, K.A., Artates, J.W., Weiss, A., Cheng, S.H., Shihabuddin, L.S.*, et al.* (2012). Sustained therapeutic reversal of Huntington's disease by transient repression of huntingtin synthesis. Neuron *74*, 1031-1044.
Lajoie, P., and Snapp, E.L. (2010). Formation and toxicity of soluble polyglutamine oligomers in living cells. PLoS One *5*, e15245.
Lanciego, J.L., Luquin, N., and Obeso, J.A. (2012). Functional neuroanatomy of the basal ganglia. Cold Spring Harb Perspect Med *2*, a009621.
Lebon, S., Bruneel, A., Drunat, S., Albert, A., Csaba, Z., Elmaleh, M., Ntorkou, A., Tenier, Y., Fenaille, F., Gressens, P.*, et al.* (2025). A biallelic variant in GORASP1 causes a novel Golgipathy with glycosylation and mitotic defects. Life Sci Alliance *8*.
Lee, H., Fenster, R.J., Pineda, S.S., Gibbs, W.S., Mohammadi, S., Davila-Velderrain, J., Garcia, F.J.,

Therrien, M., Novis, H.S., Gao, F.*, et al.* (2020). Cell Type-Specific Transcriptomics Reveals that Mutant Huntingtin Leads to Mitochondrial RNA Release and Neuronal Innate Immune Activation. Neuron *107*, 891-+.
Legleiter, J., Mitchell, E., Lotz, G.P., Sapp, E., Ng, C., DiFiglia, M., Thompson, L.M., and Muchowski, P.J. (2010). Mutant huntingtin fragments form oligomers in a polyglutamine length-dependent manner in vitro and in vivo. J Biol Chem *285*, 14777-14790.
Liu, C., Mei, M., Li, Q., Roboti, P., Pang, Q., Ying, Z., Gao, F., Lowe, M., and Bao, S. (2017). Loss of the golgin GM130 causes Golgi disruption, Purkinje neuron loss, and ataxia in mice. Proc Natl Acad Sci U S A *114*, 346-351.
Liu, J.Y., Huang, Y., Li, T., Jiang, Z., Zeng, L.W., and Hu, Z.P. (2021). The role of the Golgi apparatus in disease (Review). Int J Mol Med *47*.
Liu, Y., Chen, X., Ma, Y., Song, C., Ma, J., Chen, C., Su, J., Ma, L., and Saiyin, H. (2024). Endogenous mutant Huntingtin alters the corticogenesis via lowering Golgi recruiting ARF1 in cortical organoid. Mol Psychiatry.
Ma, L., Hu, B., Liu, Y., Vermilyea, S.C., Liu, H., Gao, L., Sun, Y., Zhang, X., and Zhang, S.C. (2012). Human embryonic stem cell-derived GABA neurons correct locomotion deficits in quinolinic acid-lesioned mice. Cell Stem Cell *10*, 455-464.
Machiela, E., and Southwell, A.L. (2020). Biological Aging and the Cellular Pathogenesis of Huntington's Disease. J Huntingtons Dis *9*, 115-128.
Martin, D.D., Ladha, S., Ehrnhoefer, D.E., and Hayden, M.R. (2015). Autophagy in Huntington disease and huntingtin in autophagy. Trends Neurosci *38*, 26-35.
Mehta, S.R., Tom, C.M., Wang, Y., Bresee, C., Rushton, D., Mathkar, P.P., Tang, J., and Mattis, V.B. (2018). Human Huntington's Disease iPSC-Derived Cortical Neurons Display Altered Transcriptomics, Morphology, and Maturation. Cell Rep *25*, 1081-1096 e1086.
Milnerwood, A.J., Cummings, D.M., Dallerac, G.M., Brown, J.Y., Vatsavayai, S.C., Hirst, M.C., Rezaie, P., and Murphy, K.P. (2006). Early development of aberrant synaptic plasticity in a mouse model of Huntington's disease. Hum Mol Genet *15*, 1690-1703.
Milnerwood, A.J., Gladding, C.M., Pouladi, M.A., Kaufman, A.M., Hines, R.M., Boyd, J.D., Ko, R.W., Vasuta, O.C., Graham, R.K., Hayden, M.R.*, et al.* (2010). Early increase in extrasynaptic NMDA receptor signaling and expression contributes to phenotype onset in Huntington's disease mice. Neuron *65*, 178-190.
Morlot, S., and Roux, A. (2013). Mechanics of dynamin-mediated membrane fission. Annu Rev Biophys *42*, 629-649.
Mukai, H., Isagawa, T., Goyama, E., Tanaka, S., Bence, N.F., Tamura, A., Ono, Y., and Kopito, R.R. (2005). Formation of morphologically similar globular aggregates from diverse aggregation-prone proteins in mammalian cells. Proc Natl Acad Sci U S A *102*, 10887-10892.
Nagai, T., Suzuki, Y., Kiyohara, H., Susa, E., Kato, T., Nagamine, T., Hagiwara, Y., Tamura, S., Yabe, T., Aizawa, C.*, et al.* (2001). Onjisaponins, from the root of Polygala tenuifolia Willdenow, as effective adjuvants for nasal influenza and diphtheria-pertussis-tetanus vaccines. Vaccine *19*, 4824-4834.
Olenick, M.A., and Holzbaur, E.L.F. (2019). Dynein activators and adaptors at a glance. J Cell Sci *132*.
Owens, G.E., New, D.M., West, A.P., and Bjorkman, P.J. (2015). Anti-PolyQ Antibodies Recognize a Short PolyQ Stretch in Both Normal and Mutant Huntingtin Exon 1. Journal of Molecular Biology

427, 2507-2519.
Passemard, S., Perez, F., Colin-Lemesre, E., Rasika, S., Gressens, P., and El Ghouzzi, V. (2017). Golgi trafficking defects in postnatal microcephaly: The evidence for "Golgipathies". Prog Neurobiol *153*, 46-63.
Peters, P.J., Ning, K., Palacios, F., Boshans, R.L., Kazantsev, A., Thompson, L.M., Woodman, B., Bates, G.P., and D'Souza-Schorey, C. (2002). Arfaptin 2 regulates the aggregation of mutant huntingtin protein. Nat Cell Biol *4*, 240-245.
Poirier, M.A., Li, H.L., Macosko, J., Cai, S.W., Amzel, M., and Ross, C.A. (2002). Huntingtin spheroids and protofibrils as precursors in polyglutamine fibrilization. Journal of Biological Chemistry *277*, 41032-41037.
Rao, S., Kirschen, G.W., Szczurkowska, J., Di Antonio, A., Wang, J., Ge, S., and Shelly, M. (2018). Repositioning of Somatic Golgi Apparatus Is Essential for the Dendritic Establishment of Adult-Born Hippocampal Neurons. J Neurosci *38*, 631-647.
Ravichandran, Y., Goud, B., and Manneville, J.B. (2020). The Golgi apparatus and cell polarity: Roles of the cytoskeleton, the Golgi matrix, and Golgi membranes. Curr Opin Cell Biol *62*, 104-113.
Sakamoto, M., Sasaki, K., Sugie, A., Nitta, Y., Kimura, T., Gursoy, S., Cinleti, T., Iai, M., Sengoku, T., Ogata, K*., et al.* (2021). De novo ARF3 variants cause neurodevelopmental disorder with brain abnormality. Hum Mol Genet *31*, 69-81.
Saudou, F., Finkbeiner, S., Devys, D., and Greenberg, M.E. (1998). Huntingtin acts in the nucleus to induce apoptosis but death does not correlate with the formation of intranuclear inclusions. Cell *95*, 55-66.
Saudou, F., and Humbert, S. (2016). The Biology of Huntingtin. Neuron *89*, 910-926.
Scherzinger, E., Sittler, A., Schweiger, K., Heiser, V., Lurz, R., Hasenbank, R., Bates, G.P., Lehrach, H., and Wanker, E.E. (1999). Self-assembly of polyglutamine-containing huntingtin fragments into amyloid-like fibrils: implications for Huntington's disease pathology. Proc Natl Acad Sci U S A *96*, 4604-4609.
Shirasaki, D.I., Greiner, E.R., Al-Ramahi, I., Gray, M., Boontheung, P., Geschwind, D.H., Botas, J., Coppola, G., Horvath, S., Loo, J.A*., et al.* (2012). Network organization of the huntingtin proteomic interactome in mammalian brain. Neuron *75*, 41-57.
Silvestroni, A., Faull, R.L., Strand, A.D., and Moller, T. (2009). Distinct neuroinflammatory profile in post-mortem human Huntington's disease. Neuroreport *20*, 1098-1103.
Sivaramakrishnan, S., Spink, B.J., Sim, A.Y., Doniach, S., and Spudich, J.A. (2008). Dynamic charge interactions create surprising rigidity in the ER/K alpha-helical protein motif. Proc Natl Acad Sci U S A *105*, 13356-13361.
Tabrizi, S.J., Flower, M.D., Ross, C.A., and Wild, E.J. (2020). Huntington disease: new insights into molecular pathogenesis and therapeutic opportunities. Nat Rev Neurol *16*, 529-546.
Takahashi, T., Kikuchi, S., Katada, S., Nagai, Y., Nishizawa, M., and Onodera, O. (2008). Soluble polyglutamine oligomers formed prior to inclusion body formation are cytotoxic. Hum Mol Genet *17*, 345-356.
Tang, C.C., Feigin, A., Ma, Y., Habeck, C., Paulsen, J.S., Leenders, K.L., Teune, L.K., van Oostrom, J.C., Guttman, M., Dhawan, V*., et al.* (2013). Metabolic network as a progression biomarker of premanifest Huntington's disease. J Clin Invest *123*, 4076-4088.
Tousley, A., Iuliano, M., Weisman, E., Sapp, E., Richardson, H., Vodicka, P., Alexander, J., Aronin, N.,

DiFiglia, M., and Kegel-Gleason, K.B. (2019). Huntingtin associates with the actin cytoskeleton and alpha-actinin isoforms to influence stimulus dependent morphology changes. Plos One *14*.
Truant, R., Atwal, R.S., Desmond, C., Munsie, L., and Tran, T. (2008). Huntington's disease: revisiting the aggregation hypothesis in polyglutamine neurodegenerative diseases. FEBS J *275*, 4252-4262.
Walker, F.O. (2007a). Huntington's disease. Lancet *369*, 218-228.
Walker, F.O. (2007b). Huntington's disease. Semin Neurol *27*, 143-150.
Wei, J.H., and Seemann, J. (2009). Mitotic division of the mammalian Golgi apparatus. Semin Cell Dev Biol *20*, 810-816.
Wu, L.L., and Zhou, X.F. (2009). Huntingtin associated protein 1 and its functions. Cell Adh Migr *3*, 71-76.
Yadav, S., and Linstedt, A.D. (2011). Golgi positioning. Cold Spring Harb Perspect Biol *3*.
Zeitlin, S., Liu, J.P., Chapman, D.L., Papaioannou, V.E., and Efstratiadis, A. (1995). Increased apoptosis and early embryonic lethality in mice nullizygous for the Huntington's disease gene homologue. Nat Genet *11*, 155-163.

Figure legends

Figure 1. Identification of a family with HD

A. The pedigree of the family with HD.

B. PCR results showed that 8 of 14 are heterogeneous; the upper band is the expanded CAGs (upper panel). Sanger sequencing revealed that the heterogeneous segment contains expanded CAG repeats (lower panel; 49 repeats; red arrows indicate the beginning and end of the CAG repeats). (See also Table S1). M, control band (CAG 35); L, Healthy local person.

C. The correlations of CAG repeat with disease onset age (Spearman's correlation).

Figure 2. Characterization of endogenous polyQ aggregate structure

A. 3B5H10 antibody and phalloidin staining showed polyQ distribution patterns in the fibroblasts of healthy (CAG 19) and patient (CAG 59). 3D-reconstructed tomography by IMARIS revealed the spatial relationships between polyQ assemblies and the nuclear surface and F-actin filaments (white arrows, polyQ puncta within the nucleus; yellow arrows, nuclear interactions). The yellow arrows in the DAPI-rendered image indicated the nuclear surface.

B. The size of polyQ assemblies in the fibroblasts of healthy siblings (n=4; cells, n=306) and HD patients (n=4; CAGs: 59, 55, 49, and 47; cells, n=783). Fiji ImageJ measured the size.

C. Average size of polyQ assembly in HD patients and healthy siblings. Student t-test; ns, $p > 0.05$.

D. Mito-tracker, phalloidin, and 3B5H10 antibody immunostaining in the fibroblasts of HD patients (CAGs, 49) and healthy siblings. 3D rendering tomography in the right two panels revealed the spatial relationships of polyQ assemblies with mitochondria and actin filaments.

E. 3B5H10 (three rights) or 3B5H10 (N-terminal) and LSB11011 (C-terminal) (left) stained polyQ puncta/patches in the mitotic cells.

F. The representative image of 3B5H10 antibodies immunostaining in HD patient (CAG 44) and healthy sibling fibroblasts by two different protocols

(immediate staining is stained 15-30 minutes after 4% PFA fixation; delayed staining is stained 48 h after 4% PFA fixation). Left panels show freshly fixed and immediately stained groups; right panels show freshly fixed and later stained groups. Images were taken by SIM microscopy with Z-stacks.

Figure 3. PolyQ assemblies of HD and healthy individuals differentially respond to stress and drugs

A. The representative polyQ assemblies in ASO-treated HD and healthy fibroblasts stained by the 3B5H10 antibody.

B, C. The changes in polyQ assembly size in ASO treatments. Comparing the trends of changes in HD with healthy (B); The changes of polyQ assembly in each individual (C) (HD, n=2 [CAG 57 and 59]; Healthy, n=2; Two-way ANOVA, * <0.05; **<0.01).

D. The immunostaining of Onjisaponin F-treated HD and healthy fibroblasts with LC-3B and 3B5H10 antibody.

E. The changes in polyQ assembly size in Onjisaponin F treatments. The trends of changes in HD and healthy individuals (HD, n=3; Healthy, n=2; Two-way ANOVA, **<0.01).

F. 3B5H10 stained polyQ assemblies under glucose starvation in the HD and healthy fibroblasts at different time points. The middle panels and the inserted image (second panel) are 3D rendering tomography in IMARIS.

G, H. The size changes of polyQ assemblies under glucose starvation in the fibroblasts of healthy siblings and HD patients at different time points. The change of polyQ assembly in the fibroblast of each individual (G) (Red line, HD patients; Green line, healthy), comparing the change of polyQ in HD with healthy (H) (Two-way ANOVA, **<0.01).

Figure 4. PolyQ assemblies circle the large Golgi apparatus

A. GM130 and 3B5H10 antibodies and phalloidin staining in healthy sibling and HD fibroblasts showed that polyQ assemblies circle the Golgi apparatus (z-stack intervals, 0.2μm). The rendering tomography of Z-stacked images

revealed the spatial relationship of polyQ assemblies with the Golgi stack; polyQ assemblies circle the Golgi stack, and a narrowing of GM130-stained Golgi exists in the site where polyQ encircles the Golgi (yellow arrows, isthmus; blue arrows, the arm of polyQ; the boxed region, the magnified part in the right panel).

B. The size of the GM130-stained Golgi apparatus in HD and healthy individuals (HD, n=3; Healthy, n=3. Student *t*-test; **<0.01).

C. The representative images of clathrin and 3B5H10 antibody immunostaining in the fibroblasts of an HD patient and healthy fibroblasts. The left is a large polyQ assembly. The inner inserts on the left show angled and rendered views of the spatial relationship between the polyQ assembly and clathrin+ puncta. The right is the interacting pattern of polyQ with the nucleus and attaching patterns of clathrin to polyQ assemblies that interact with the nucleus (inner inserts, rendered view [lower] and the conjugation pattern of clathrin with polyQ assembly [upper]).

D. The number of Clathrin^{+} vesicles overlapped with polyQ assemblies. The object-object statistics in IMARIS were used to measure overlapping. HD, n=3; Healthy, n=3. Data, mean± SD. Student *t*-test; *<0.05.

E. HTT C-terminal antibody and polyQ antibody immunostaining revealed that C-terminal antibody signals colocalize with cytoplasmic polyQ assemblies.

F. Coimmunostaining of 3B5H10 antibody with HAP40 antibody revealed that polyQ assemblies were attached by HAP40. The lefts are sectional views, and the rights are 3D renderings of the middle panel by IMARIS surface.

G. The count of HAP40 puncta attached to polyQ assemblies in healthy and HD fibroblasts. The distances between HAP40 puncta and polyQ assemblies were measured by IMARIS. HD, n=2; Healthy, n=2. Student t-test; Data, mean ± SD. Student t-test; ns, p>0.05

H. The 3B5H10 and GM130 antibodies immunostaining images in the mitotic fibroblasts, including prometaphase, anaphase, and telophase, were obtained by SIM microscopy. The inserted DAPI images (gray) showed the nuclear

chromatin structure. The right panels are a sectional view of the boxed region (anaphase and telophase).

I. ARF1 and 3B5H10 antibody immunostaining in the fibroblasts revealed that ARF1 preferentially interacts with polyQ assemblies.

J. The measurement of polyQ assembly-conjugated AFR1 puncta in the healthy and HD fibroblasts. Student t-test; **<0.001

K. GM130 and 3B5H10 antibody immunostaining in BFA-treated fibroblasts revealed that most fragmented Golgi liberate from polyQ. The boxed region in the upper panel is the magnified region. The lower insert is a 3D rendering of a tomographic image.

L. The volume of polyQ assemblies/puncta in fibroblasts after 2 hours and 7 hours of treatment by BFA. The measurements were performed using IMARIS software. (Images, n: 7-12. Sample size: n=2 in each group. One-way ANOVA, **<0.01).

M. The count of 3B5H10-stained assemblies/puncta in the fibroblasts (Images, n: 7-11. Sample size: n=2 in each group. One-way ANOVA, **<0.01).

N. Image sequences of Golgi labelled by GOLGI ID Green assay kit in the living fibroblasts of healthy siblings and HD patients (CAG 59, 49, and CAG 49) after glucose starvation (The displays, the inverted channel of the original image).

O. The fragmentation ratio of the Golgi under glucose starvation at different time points in healthy and HD fibroblasts. Fragmentation ratio = number of Golgi of a cell at each time point/ number of Golgi at 0 min (Two-way ANOVA. **<0.01. The number of images in the cell line: n>5).

Fig. 5. The characteristics of polyQ assembly in the induced striatal and cortical neurons

A. The characteristics of polyQ assembly in iPS -derived striatal GABAergic neurons at day 90 and 120 (i, the nucleus without nuclear accumulation; ii, the nucleus with nuclear polyQ accumulation). The inner inserts show the 3D tomographic rendering, which revealed the spatial relationship between polyQ

assemblies and the nucleus.

B. The size of polyQ assemblies in iPSCs-derived GABAergic neurons (HD, n=4 [CAG 59, 55, 49, and 47]; Healthy, n=3 [CAG 19, CAG 19, and H9]). Data, mean ± SD. t-test; **<0.01.

C. The percentage of nuclear polyQ volume/total polyQ volume in iPS-derived GABAergic neuronal nucleus cultured over 90 days (HD, n=4 [CAG 59, 55, 49, and 47]; Healthy, n=3 [CAG 19, CAG 19, and H9]). *t*-test; **<0.01.

D. The representative images of polyQ assemblies and Golgi stained by 3B5H10 and GM130 antibodies in hCO (Taken by SIM microscopy; Z-stack interval, 0.2μm). The right panels show the rendered tomography of the Golgi by Imaris 9.8 surface (white arrows indicate the Golgi with an irregular surface).

E. The representative images of polyQ assemblies and Golgi stained by 3B5H10 and GM130 antibodies in hStrO (taken by SIM microscopy; Z-stack interval, 0.2 μm). The middle panels are a sectional view of the rectangle. The lower panels are 3D rendering tomography by Imaris 9.8 surface.

F. Comparing the overlapped volume of the Golgi with polyQ assemblies in HD striatal neurons with that of healthy striatal neurons. The object-object statistic function in Imaris 9.8 measures the overlapped volume (Student *t*-test; **, p <0.01. HD hStrO: CAG 55 and CAG 47; Healthy hStrO: H9, CAG 19. Student *t*-test, *<0.05).

G. The images of polyQ assemblies stained by 3B5H10 and clathrin antibodies in hStrOs were taken by SIM microscopy (The upper panel, the lateral view of the boxed region; the inner insert in the rendered image, a larger view of the original image). The renderings are done by Imaris surface.

H. Comparing clathrin+ vesicle volume overlapped with 3B5H10-stained polyQ assemblies of striatal neurons in the healthy sibling with an HD patient. *t*-test, *, p<0.05. HD hStrO: CAG 55 and CAG 47; Healthy hStrO: H9, CAG 19. Student *t*-test; * <0.05.

I. 3B5H10 and GM130 antibodies immunostaining images and their sectional

views in the neurons of hStrO of HD patients and healthy siblings revealed the spatial relationships between polyQ assemblies and Golgi (white arrows, the Golgi in the inner hole of the ring; pink arrows, the scaffolding Golgi; the boxed region, the right or left panel). The right panel is a 3B5H10-stained assembly in a human striatal neuron with a long projection.

J. 3B5H10 and clathrin antibodies staining images of the neurons in hStrO of HD patients and healthy siblings revealed the spatial relationships between polyQ assemblies and clathrin-stained vesicles. The left panel is a sectional view between two arrows (hStrO at day 80; two white arrows, the segment in the right panel)

K. The raster plots and network activity of the cortical neurons in HD and healthy hCOs.

L. Quantification of network features at the burst level in HD and healthy hCOs, including the number of spikes per burst, the interburst intervals (IBI), and IBI CV (CTR group: n=3 hCOs; HD group: n=3 hCOs; The mean ± SD, Welch's t-test, * < 0.05; ** < 0.01).

Fig. 6. GABAergic neurons from HD patients reduced Golgi- or vesicle-related activities and intensified nucleus-related activities

A, B. Uniform manifold approximation and projection (UMAP) plot of all cells colored by their sample origin (A) and by cell types(B).

C. Dot plot displaying an expression of example marker genes.

D. Venn diagram summarizing the number of overlapped genes differentially expressed in CAG59 vs. CAG19/H9 GABAergic neurons.

E. GO enrichment analysis of down-regulated (top) and up-regulated (bottom) genes in CAG59 vs. CAG19/H9 GABAergic neurons.

Figure 7. Onjisaponin F did not mitigate polyQ nuclear accumulation, and ASO corrected the aberrant HD striatal neuronal firing

A. The schematics of treatment (upper) and the representative images of polyQ assemblies stained by 3B5H10 antibodies in HD and healthy striatal neurons at 63 days treated by one dose of 20 μM onjisaponin F for 72 h.

Fig.1

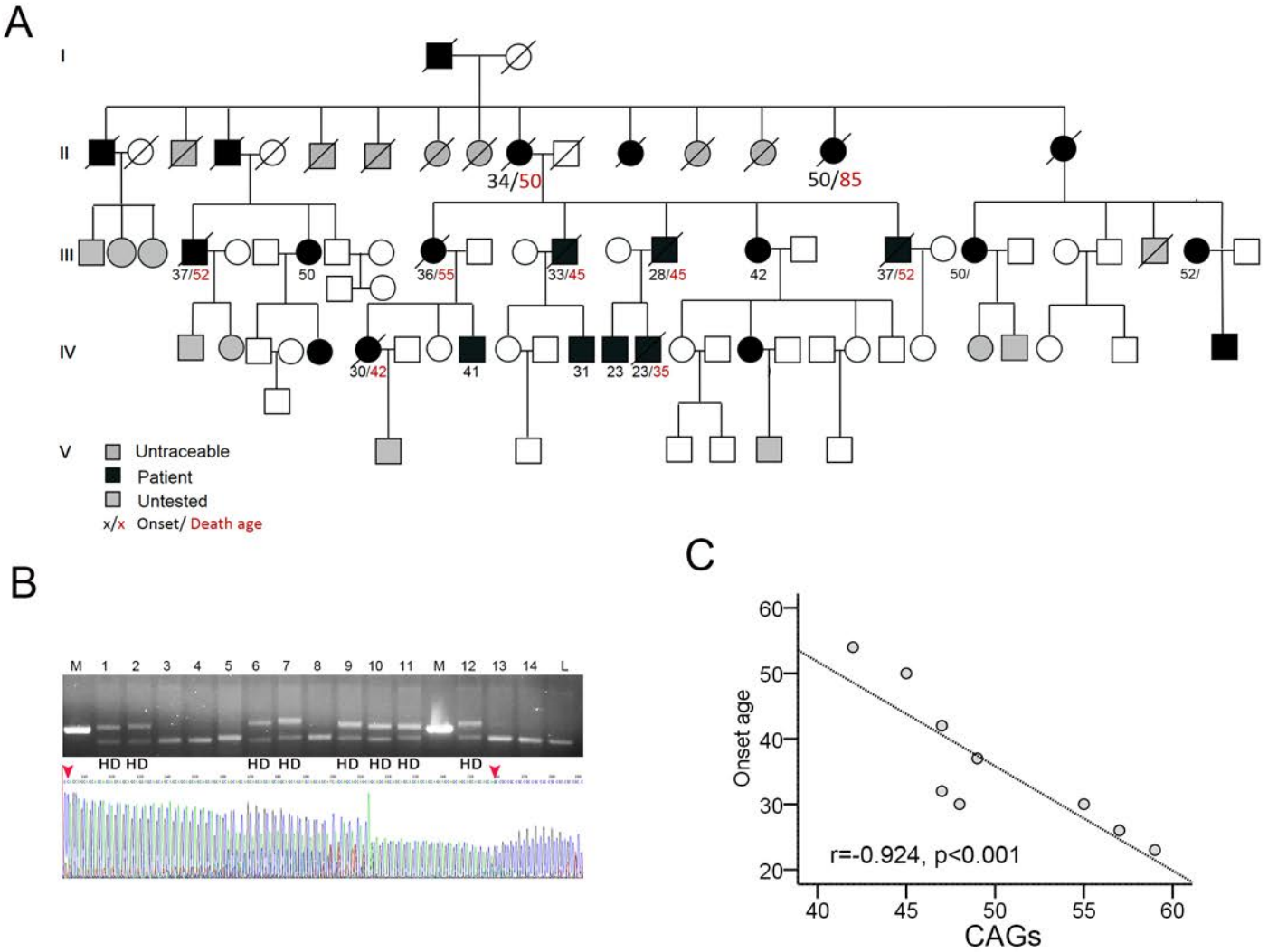
A
I
II
III
IV
V
34/50
50/85
37/52
50
36/55
33/45
28/45
42
37/52
50/
52/
30/42
41
31
23
23/35
Untraceable
Patient
Untested
x/x Onset/ Death age
B
M 1 2 3 4 5 6 7 8 9 10 11 M 12 13 14 L
HD HD
HD HD
HD HD HD
HD
C
Onset age
CAGs
r=-0.924, p<0.001
60
50
40
30
20
40
45
50
55
60

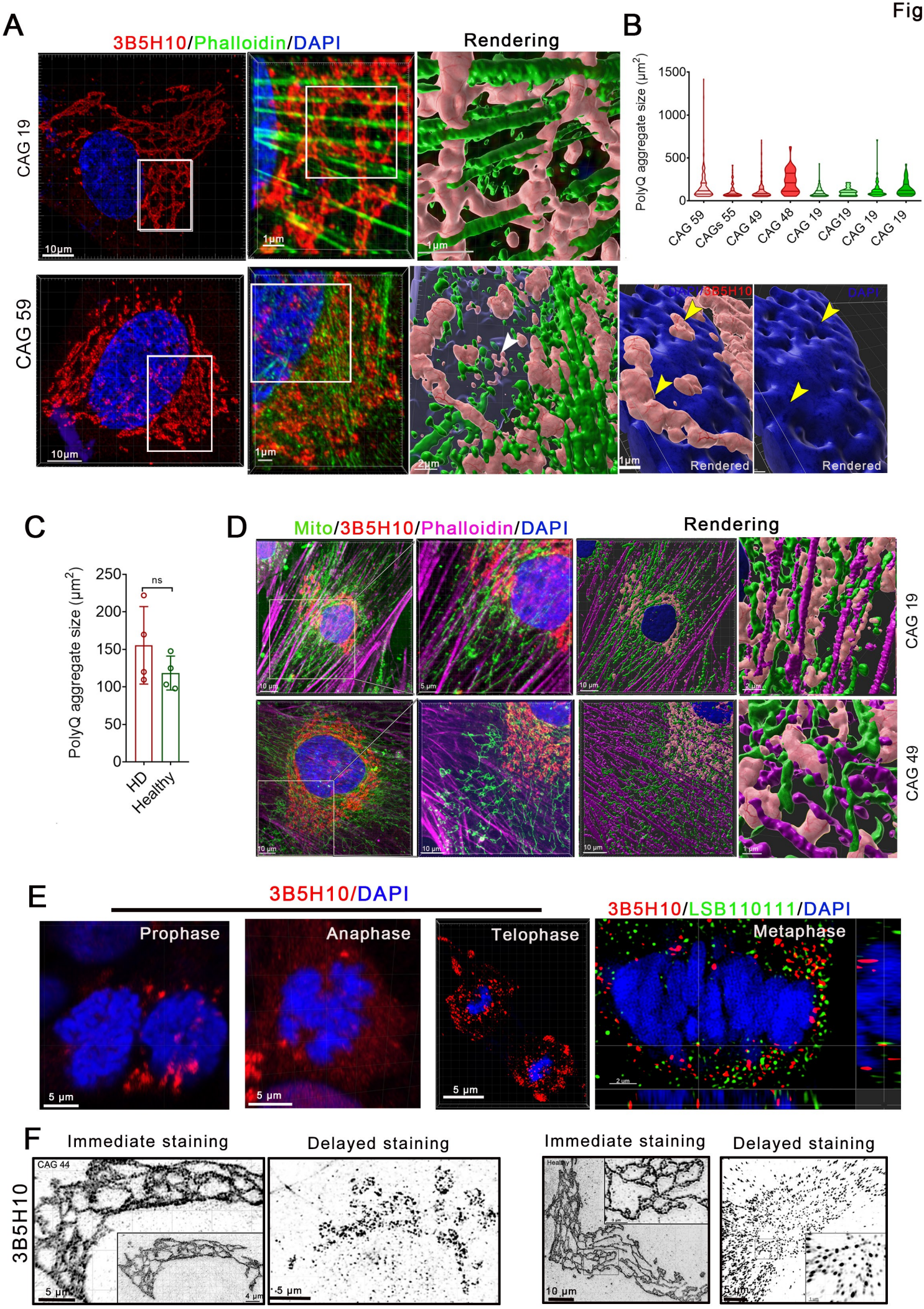
A
3B5H10/Phalloidin/DAPI
Rendering
CAG 19
CAG 59
10µm
1µm
2µm
B
PolyQ aggregate size (µm²)
1500
1000
500
0
CAG 59
CAGs 55
CAG 49
CAG 48
CAG 19
CAG19
CAG 19
CAG 19
3B5H10
DAPI
Rendered
C
PolyQ aggregate size (µm²)
250
200
150
100
50
0
ns
HD
Healthy
D
Mito/3B5H10/Phalloidin/DAPI
Rendering
CAG 19
CAG 49
10 µm
5 µm
1 µm
E
3B5H10/DAPI
3B5H10/LSB110111/DAPI
Prophase
Anaphase
Telophase
Metaphase
5 µm
2 µm
F
Immediate staining
Delayed staining
Immediate staining
Delayed staining
3B5H10
CAG 44
Healthy
5 µm
4 µm
10 µm

Fig.3

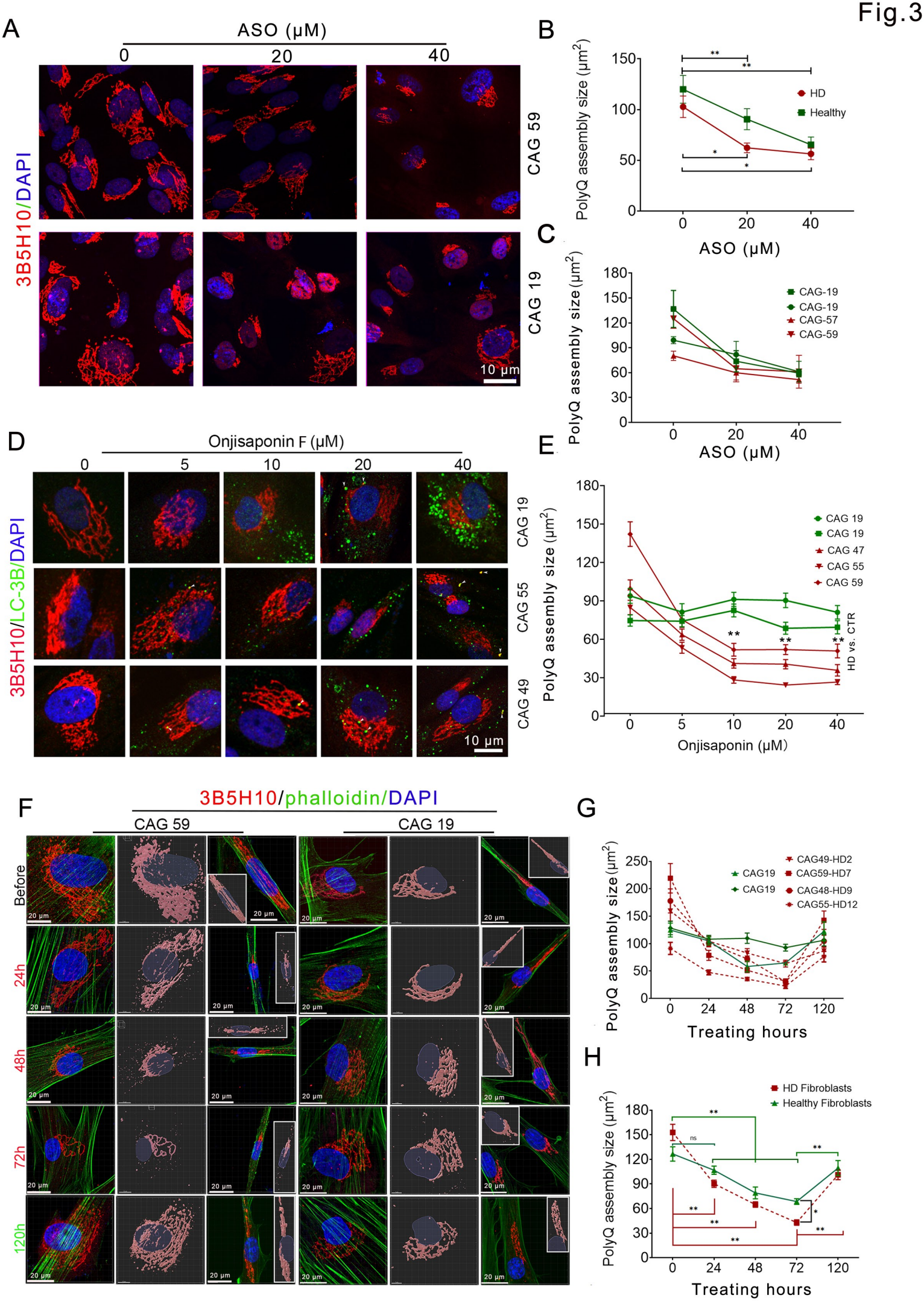
A
ASO (μM)
0
20
40
3B5H10/DAPI
CAG 59
CAG 19
10 μm
B
PolyQ assembly size (μm²)
HD
Healthy
ASO (μM)
C
PolyQ assembly size (μm²)
CAG-19
CAG-19
CAG-57
CAG-59
ASO (μM)
D
Onjisaponin F (μM)
0
5
10
20
40
3B5H10/LC-3B/DAPI
CAG 19
CAG 55
CAG 49
10 μm
E
PolyQ assembly size (μm²)
CAG 19
CAG 19
CAG 47
CAG 55
CAG 59
HD vs. CTR
Onjisaponin (μM)
F
3B5H10/phalloidin/DAPI
CAG 59
CAG 19
Before
24h
48h
72h
120h
20 μm
G
PolyQ assembly size (μm²)
CAG19
CAG19
CAG49-HD2
CAG59-HD7
CAG48-HD9
CAG55-HD12
Treating hours
H
PolyQ assembly size (μm²)
HD Fibroblasts
Healthy Fibroblasts
ns
Treating hours

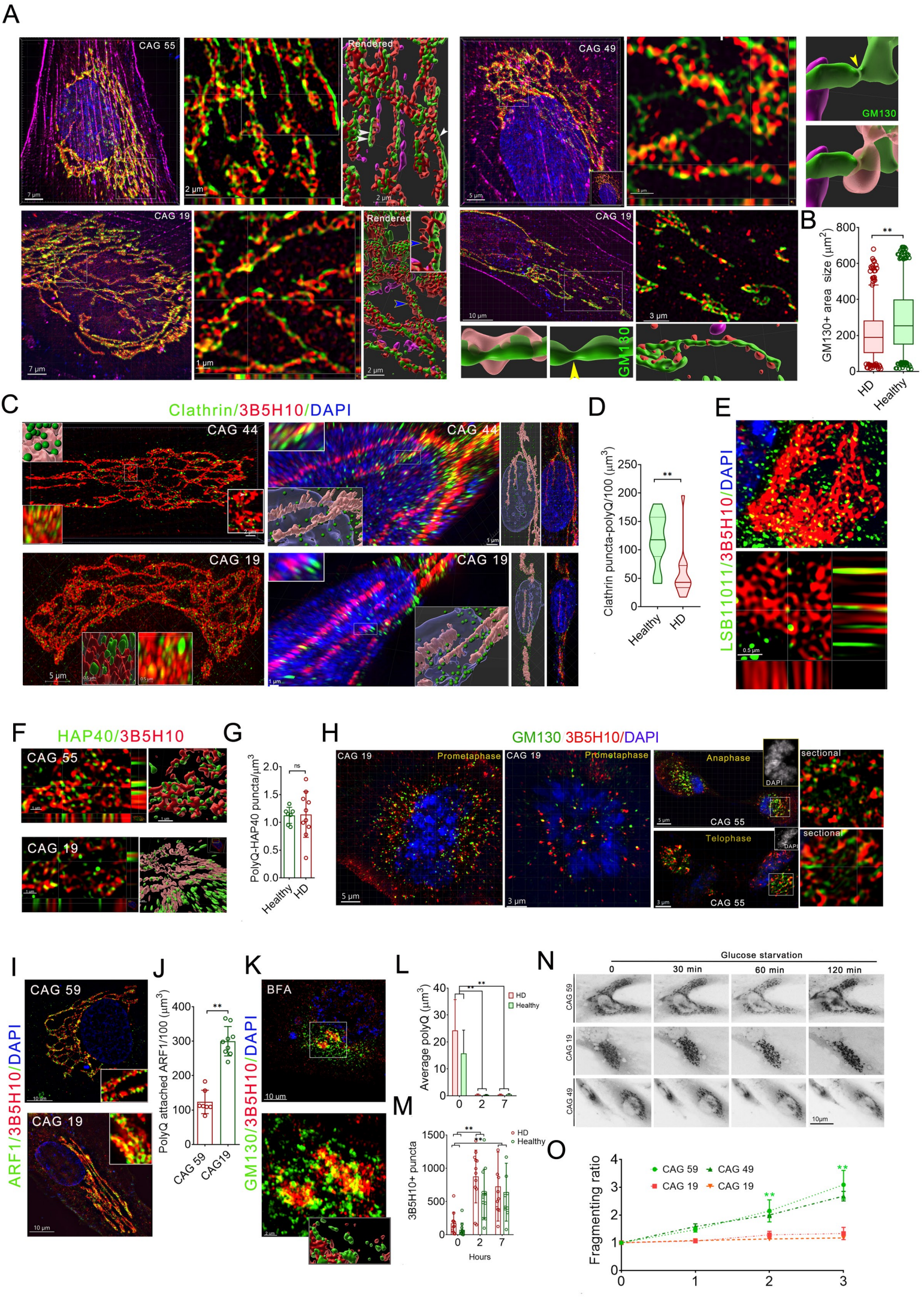
A
CAG 55
Rendered
CAG 49
GM130
CAG 19
Rendered
CAG 19
GM130
B
GM130+ area size (μm²)
HD
Healthy
C
Clathrin/3B5H10/DAPI
CAG 44
CAG 44
CAG 19
CAG 19
D
Clathrin puncta-polyQ/100 (μm³)
Healthy
HD
E
LSB11011/3B5H10/DAPI
F
HAP40/3B5H10
CAG 55
CAG 19
G
PolyQ-HAP40 puncta/μm³
ns
Healthy
HD
H
GM130 3B5H10/DAPI
CAG 19
Prometaphase
CAG 19
Prometaphase
Anaphase
DAPI
CAG 55
sectional
Telophase
DAPI
CAG 55
sectional
I
ARF1/3B5H10/DAPI
CAG 59
CAG 19
J
PolyQ attached ARF1/100 (μm³)
CAG 59
CAG19
K
BFA
GM130/3B5H10/DAPI
L
Average polyQ (μm³)
HD
Healthy
M
3B5H10+ puncta
HD
Healthy
Hours
N
Glucose starvation
0
30 min
60 min
120 min
CAG 59
CAG 19
CAG 49
O
Fragmenting ratio
CAG 59
CAG 49
CAG 19
CAG 19

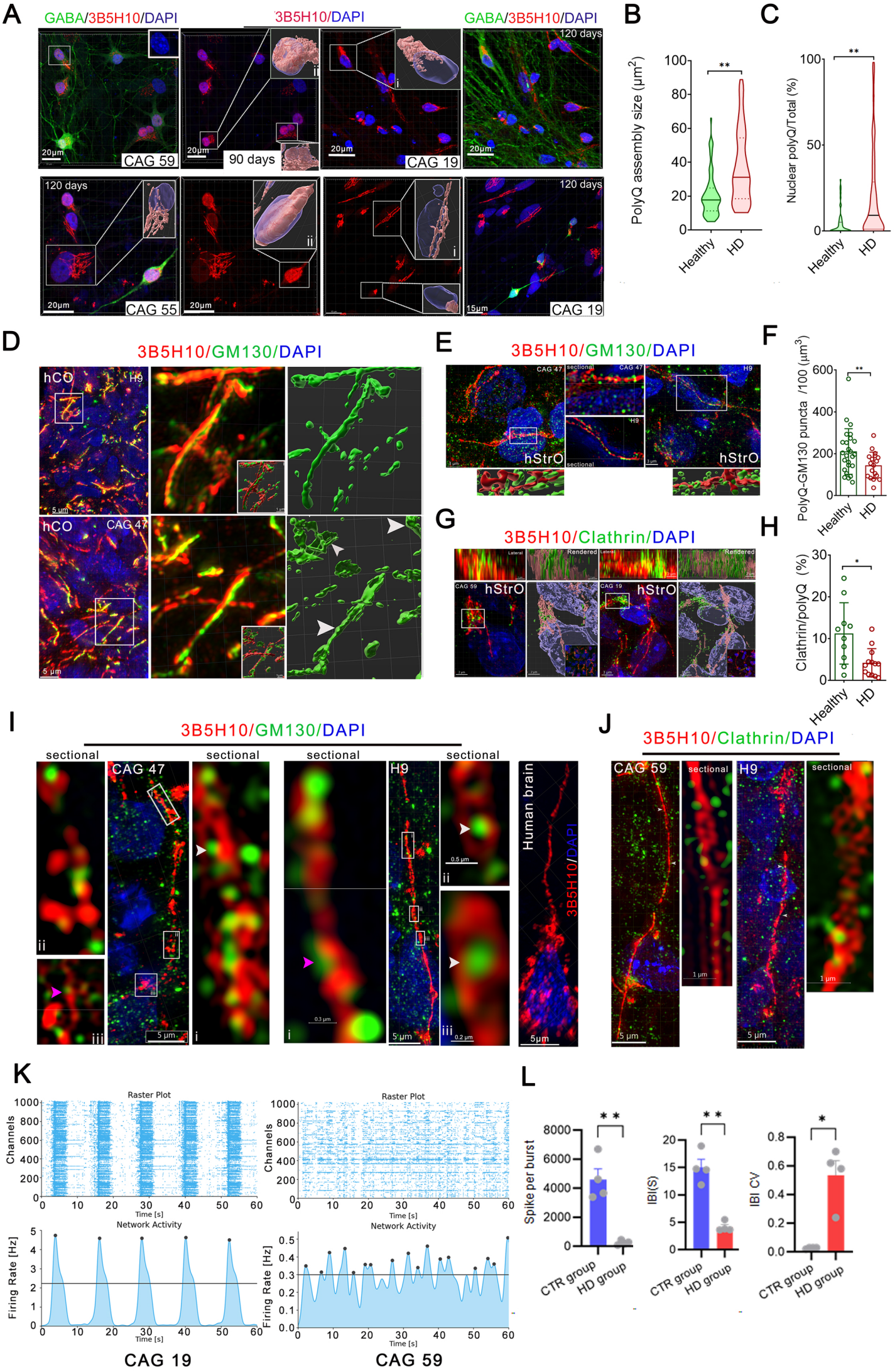
A
GABA/3B5H10/DAPI
3B5H10/DAPI
GABA/3B5H10/DAPI
CAG 59
90 days
CAG 19
120 days
CAG 55
CAG 19
B
PolyQ assembly size (μm²)
Healthy
HD
C
Nuclear polyQ/Total (%)
Healthy
HD
D
3B5H10/GM130/DAPI
hCO
H9
CAG 47
E
3B5H10/GM130/DAPI
hStrO
F
PolyQ-GM130 puncta /100 (μm³)
Healthy
HD
G
3B5H10/Clathrin/DAPI
hStrO
H
Clathrin/polyQ (%)
Healthy
HD
I
3B5H10/GM130/DAPI
sectional
CAG 47
H9
Human brain
3B5H10/DAPI
J
3B5H10/Clathrin/DAPI
CAG 59
H9
sectional
K
Raster Plot
Channels
Time [s]
Network Activity
Firing Rate [Hz]
CAG 19
CAG 59
L
Spike per burst
IBI(S)
IBI CV
CTR group
HD group

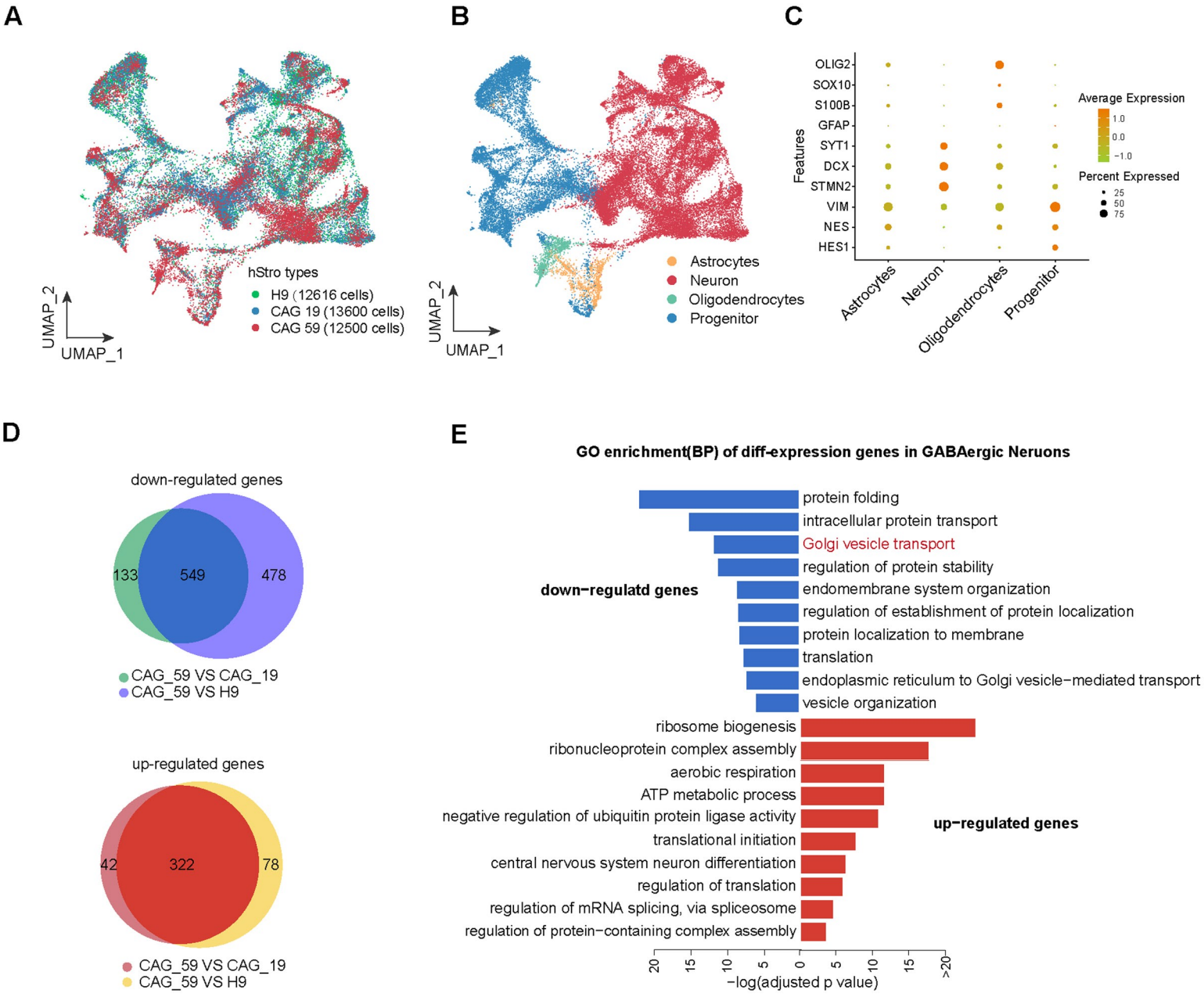
A
hStro types
H9 (12616 cells)
CAG 19 (13600 cells)
CAG 59 (12500 cells)
UMAP_2
UMAP_1
B
Astrocytes
Neuron
Oligodendrocytes
Progenitor
UMAP_2
UMAP_1
C
OLIG2
SOX10
S100B
GFAP
SYT1
DCX
STMN2
VIM
NES
HES1
Features
Astrocytes
Neuron
Oligodendrocytes
Progenitor
Average Expression
1.0
0.0
−1.0
Percent Expressed
25
50
75
D
down-regulated genes
133
549
478
CAG_59 VS CAG_19
CAG_59 VS H9
up-regulated genes
42
322
78
CAG_59 VS CAG_19
CAG_59 VS H9
E
GO enrichment(BP) of diff-expression genes in GABAergic Neruons
down−regulatd genes
protein folding
intracellular protein transport
Golgi vesicle transport
regulation of protein stability
endomembrane system organization
regulation of establishment of protein localization
protein localization to membrane
translation
endoplasmic reticulum to Golgi vesicle−mediated transport
vesicle organization
up−regulated genes
ribosome biogenesis
ribonucleoprotein complex assembly
aerobic respiration
ATP metabolic process
negative regulation of ubiquitin protein ligase activity
translational initiation
central nervous system neuron differentiation
regulation of translation
regulation of mRNA splicing, via spliceosome
regulation of protein−containing complex assembly
20
15
10
5
0
5
10
15
>20
−log(adjusted p value)

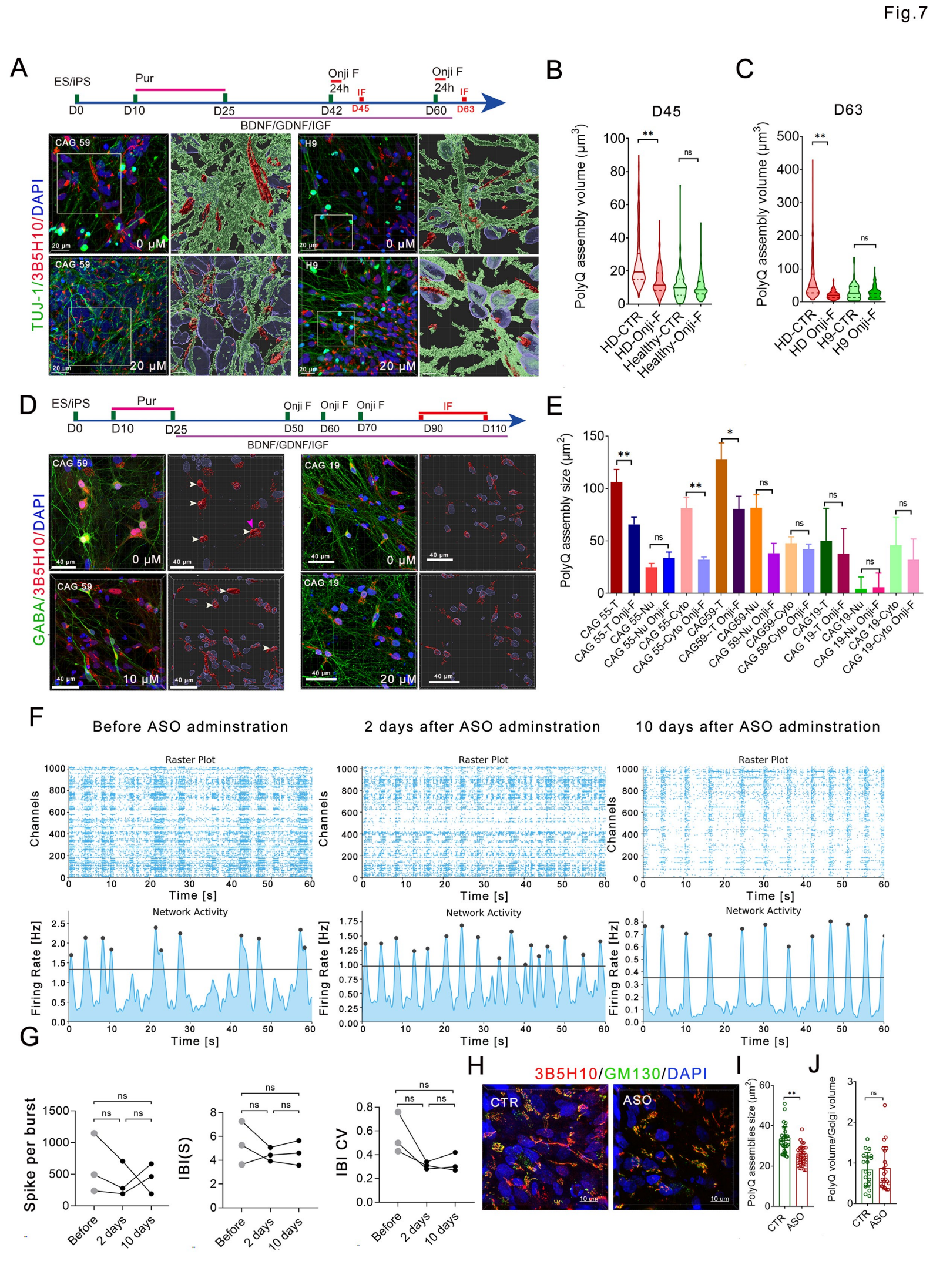
A
ES/iPS
Pur
Onji F
24h
IF
D0
D10
D25
D42
D45
D60
D63
BDNF/GDNF/IGF
TUJ-1/3B5H10/DAPI
CAG 59
H9
0 μM
20 μM
B
D45
PolyQ assembly volume (μm3)
HD-CTR
HD-Onji-F
Healthy-CTR
Healthy-Onji-F
C
D63
HD Onji-F
H9-CTR
H9 Onji-F
D
D50
D60
D70
D90
D110
GABA/3B5H10/DAPI
CAG 19
10 μM
E
PolyQ assembly size (μm2)
CAG 55-T
CAG 55-T Onji-F
CAG 55-Nu
CAG 55-Nu Onji-F
CAG 55-Cyto
CAG 55-Cyto Onji-F
CAG59-T
CAG59-T Onji-F
CAG59-Nu
CAG 59-Nu Onji-F
CAG59-Cyto
CAG 59-Cyto Onji-F
CAG19-T
CAG 19-T Onji-F
CAG19-Nu
CAG 19-Nu Onji-F
CAG 19-Cyto
CAG 19-Cyto Onji-F
F
Before ASO adminstration
2 days after ASO adminstration
10 days after ASO adminstration
Raster Plot
Channels
Time [s]
Network Activity
Firing Rate [Hz]
G
Spike per burst
IBI(S)
IBI CV
Before
2 days
10 days
H
3B5H10/GM130/DAPI
CTR
ASO
I
PolyQ assemblies size (μm2)
J
PolyQ volume/Golgi volume

S-table-1. The baseline characteritics of HD family members

No	Gender	Age	F	Onset age	CAG (mutant)	CAG (wild)	Syndrome (on sampling age)	Death	Sampling year
1	F	46	F3	42	47	19	moderate		2010
2	M	44	F3	37	49	19	moderate	54	2010
3	M	21	F4			19			2010
4	F	28	F4			19			2010
5	F	26	F4			19			2010
6	M	23	F4	26	57	19	mild		2010
7	M	27	F4	23	59	19	mild	36	2010
8	F	19	F4			19			2010
9	M	28	F4	30	48	19	mild		2010
10	F	26	F4	32	47	19	no syndrome		2010
11	M	5	F5		45	18	no syndrome		2010
12	F	39	F4	30	55	19	critical	42	2010
13	F	42	F4			19			2010
14	F	23	F4			19			2010
15	M	44	F4	41	NA		critical		2010
16	M	17	F5		NA				2010
17	M	33	F4			19			2017
18	F	30	F3		45	19	no syndrome		2017
19	F	52	F4		45	19	moderate		2017
20	F	25	F3			19			2017
21	M	21	F3			19			2017
22	M	52	F2		NA		died without syndrome		2019
23	M	30	F4		44	19	no syndrome		2019
24	F	54	F3		42	19	moderate		2019
25	F	56	F3		NA		critical		2020
26	M	52	F3		NA		healthy		2020
27	F	28	F4		NA		healthy		2020
28	M	32	F4		NA		healthy		2020

F, female; M,male; NA, non-assessed; F1-4 genereation

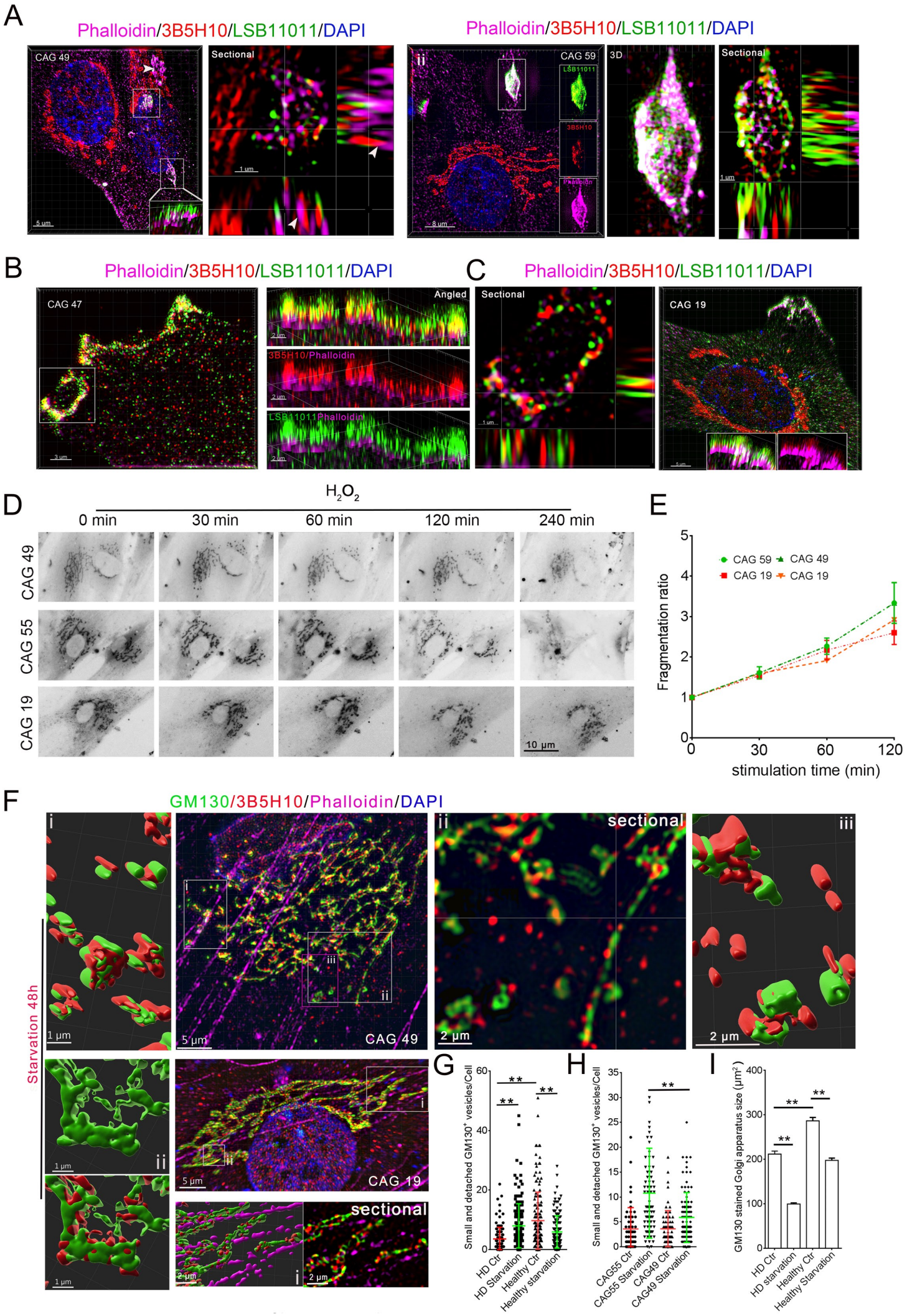
A
Phalloidin/3B5H10/LSB11011/DAPI
CAG 49
Sectional
Phalloidin/3B5H10/LSB11011/DAPI
CAG 59
LSB11011
3B5H10
Phalloidin
3D
Sectional
B
Phalloidin/3B5H10/LSB11011/DAPI
CAG 47
Angled
3B5H10/Phalloidin
LSB11011/Phalloidin
C
Phalloidin/3B5H10/LSB11011/DAPI
Sectional
CAG 19
D
H2O2
0 min
30 min
60 min
120 min
240 min
CAG 49
CAG 55
CAG 19
10 µm
E
Fragmentation ratio
CAG 59
CAG 49
CAG 19
CAG 19
stimulation time (min)
F
GM130/3B5H10/Phalloidin/DAPI
Starvation 48h
CAG 49
CAG 19
sectional
G
Small and detached GM130+ vesicles/Cell
HD Ctr
HD Starvation
Healthy Ctr
Healthy starvation
H
Small and detached GM130+ vesicles/Cell
CAG55 Ctr
CAG55 Starvation
CAG49 Ctr
CAG49 Starvation
I
GM130 stained Golgi apparatus size (µm2)
HD Ctr
HD starvation
Healthy Ctr
Healthy Starvation

A

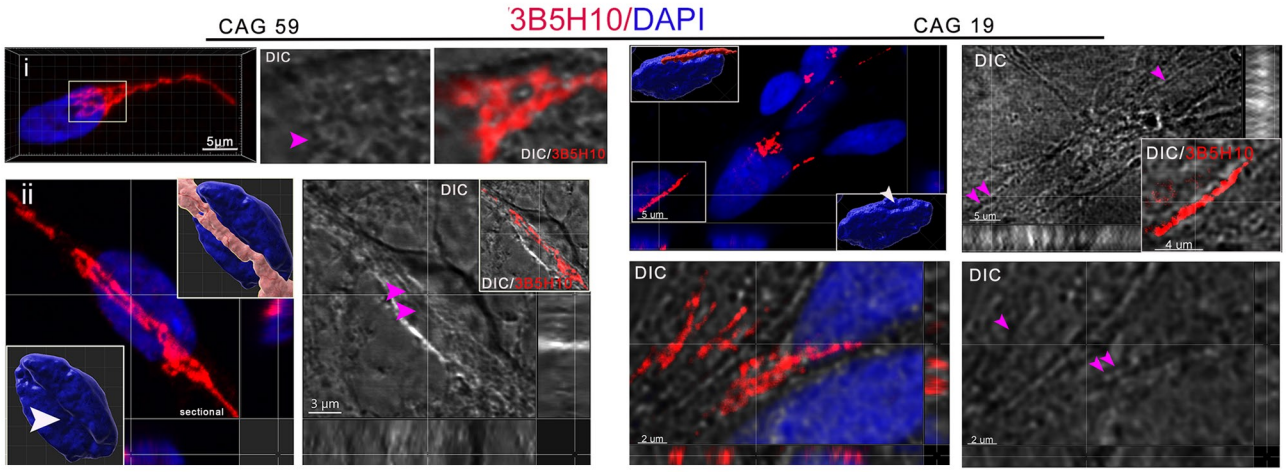

B

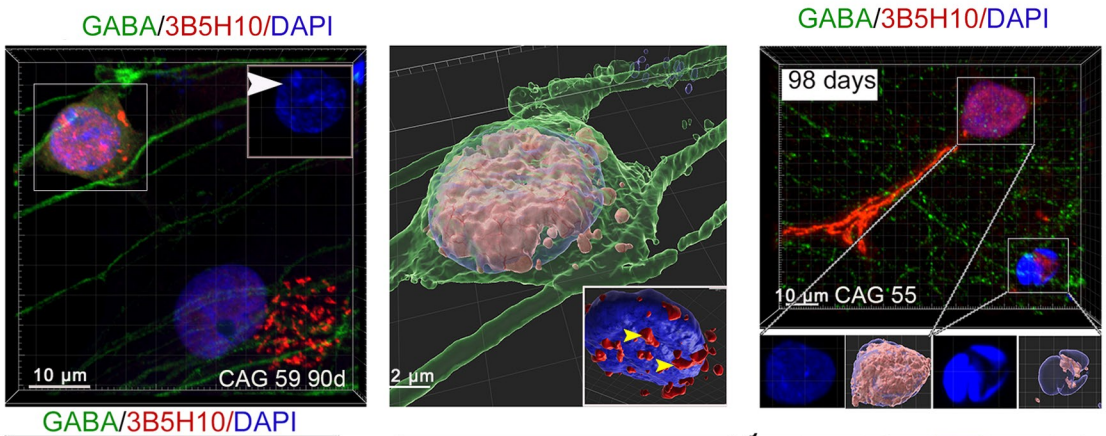

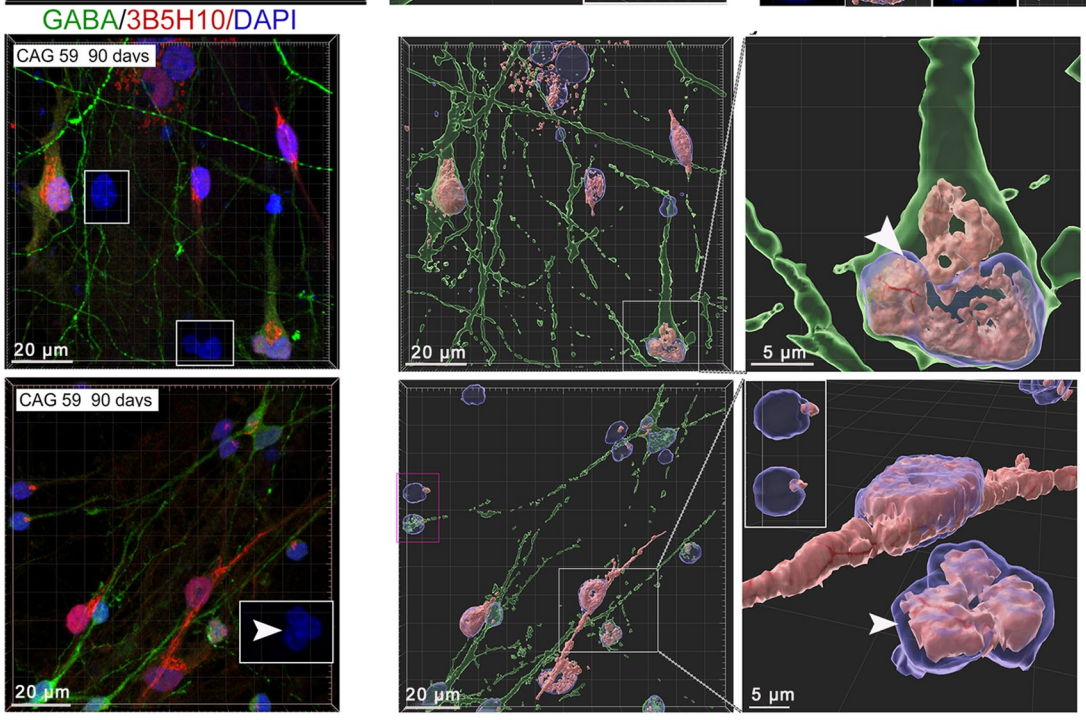

C

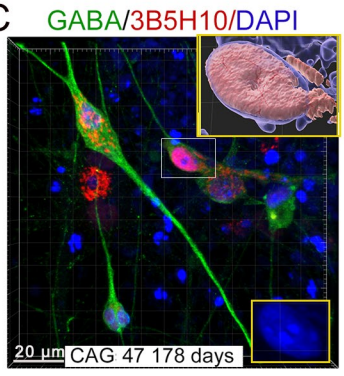

D

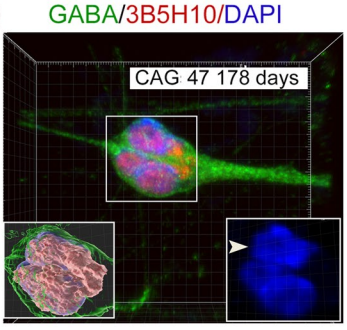

E

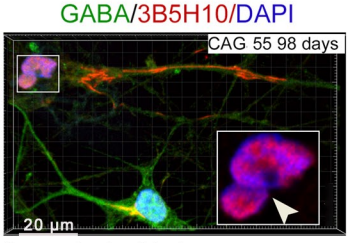

Summary of nuclear slicing in neruons

HD	Nuclear slicing	Total neurons	Image number
CAG 59	6	224	34
CAG 55	4	178	29
CAG 47	8	201	27

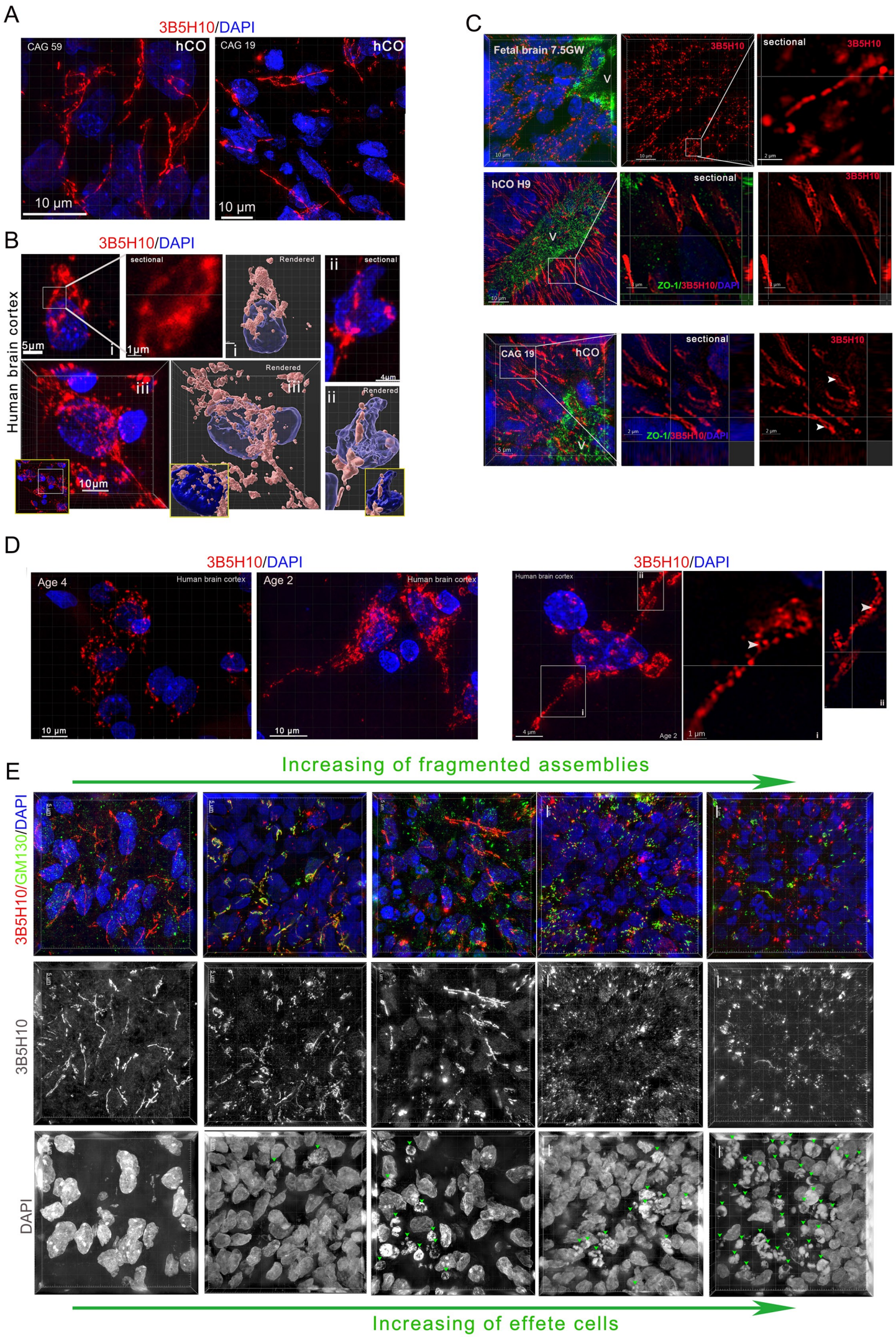
A
3B5H10/DAPI
CAG 59
hCO
CAG 19
hCO
10 µm
10 µm
B
3B5H10/DAPI
Human brain cortex
sectional
Rendered
sectional
5µm
1µm
4µm
10µm
Rendered
Rendered
C
Fetal brain 7.5GW
3B5H10
sectional
3B5H10
V
hCO H9
sectional
3B5H10
V
ZO-1/3B5H10/DAPI
CAG 19
hCO
sectional
3B5H10
V
ZO-1/3B5H10/DAPI
D
3B5H10/DAPI
Age 4
Human brain cortex
Age 2
Human brain cortex
10 µm
10 µm
3B5H10/DAPI
Human brain cortex
Age 2
1 µm
E
Increasing of fragmented assemblies
3B5H10/GM130/DAPI
3B5H10
DAPI
Increasing of effete cells

A

human Striatal Organoids

GSH2/MASH1/DAPI

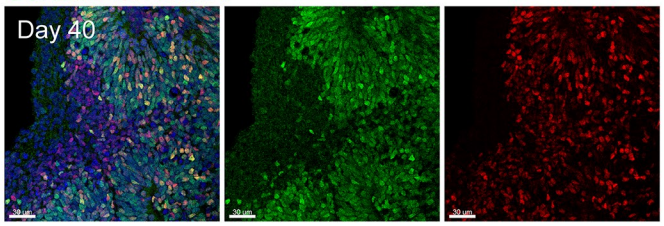

DARPP32/CTIP2/DAPI

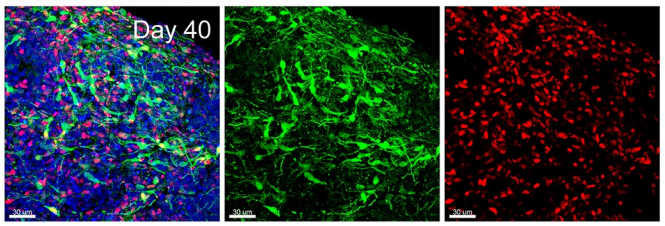

B

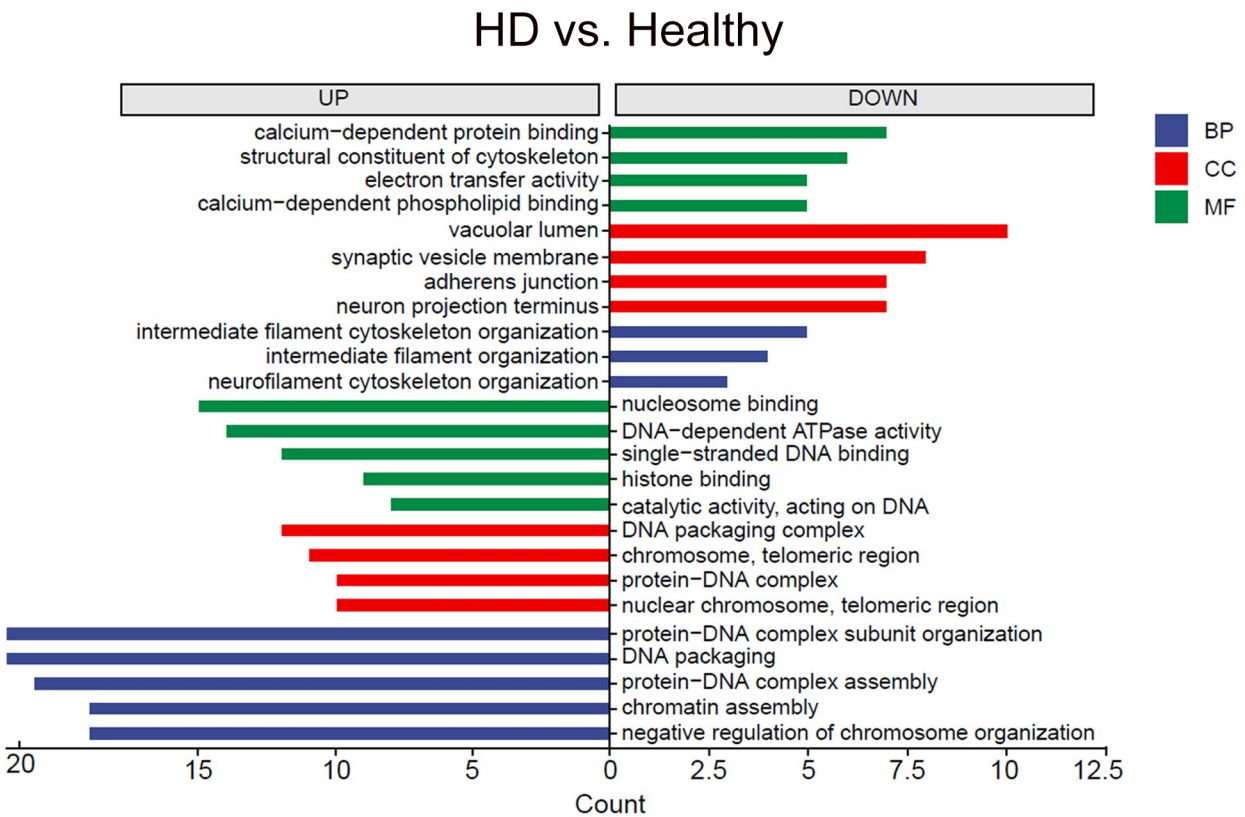

C

human Cortical Organoids

PAX6/TBR2/HOPX/DAPI

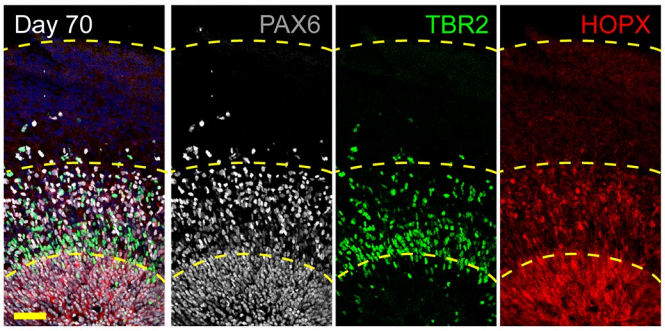

TBR1/CTIP2/SATB2/DAPI

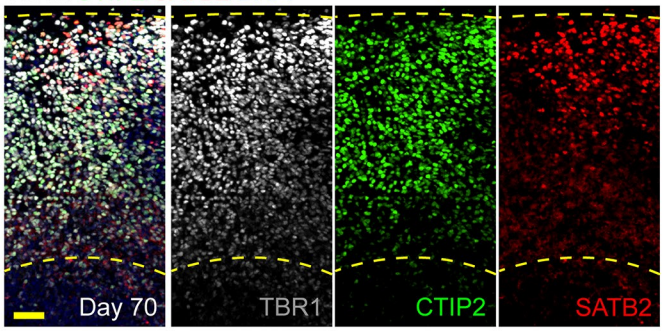

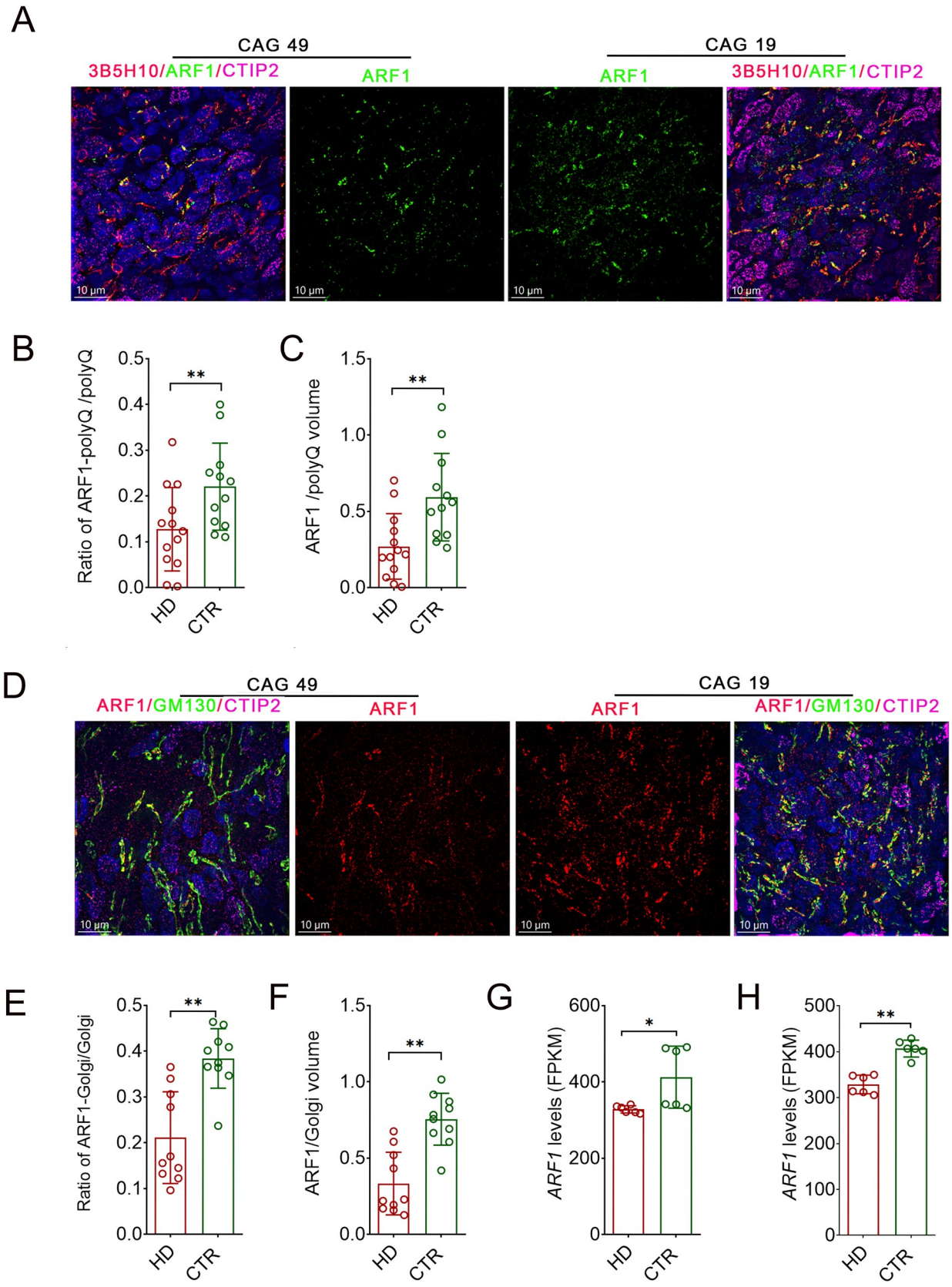
A
CAG 49
CAG 19
3B5H10/ARF1/CTIP2
ARF1
ARF1
3B5H10/ARF1/CTIP2
10 μm
B
Ratio of ARF1-polyQ /polyQ
C
ARF1 /polyQ volume
HD
CTR
D
CAG 49
CAG 19
ARF1/GM130/CTIP2
ARF1
ARF1
ARF1/GM130/CTIP2
E
Ratio of ARF1-Golgi/Golgi
F
ARF1/Golgi volume
G
ARF1 levels (FPKM)
H
ARF1 levels (FPKM)

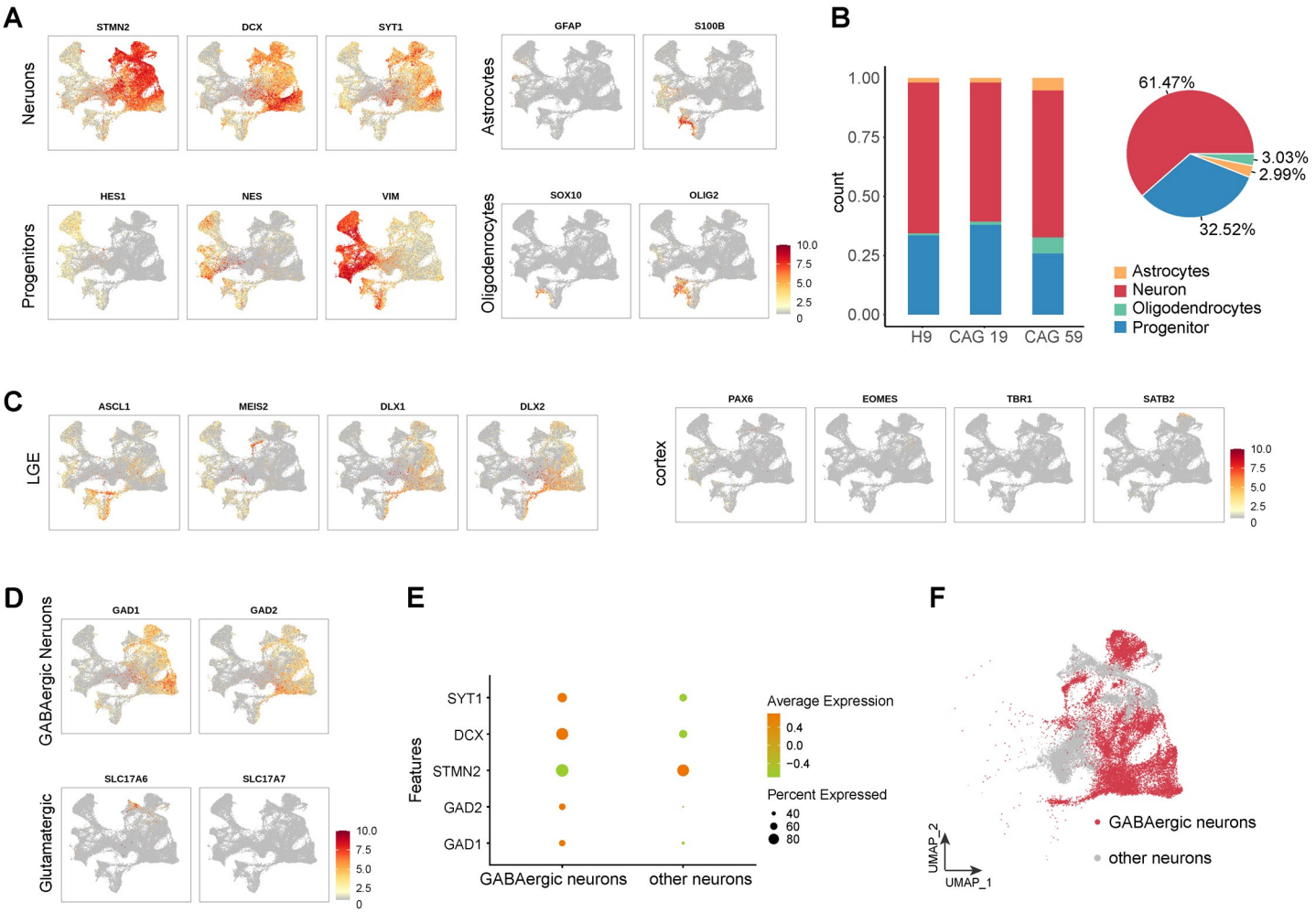
A
STMN2
DCX
SYT1
GFAP
S100B
Neruons
Astrocytes
HES1
NES
VIM
SOX10
OLIG2
Progenitors
Oligodenrocytes
10.0
7.5
5.0
2.5
0
B
count
1.00
0.75
0.50
0.25
0.00
H9
CAG 19
CAG 59
61.47%
3.03%
2.99%
32.52%
Astrocytes
Neuron
Oligodendrocytes
Progenitor
C
ASCL1
MEIS2
DLX1
DLX2
LGE
PAX6
EOMES
TBR1
SATB2
cortex
D
GAD1
GAD2
GABAergic Neruons
SLC17A6
SLC17A7
Glutamatergic
E
Features
SYT1
DCX
STMN2
GAD2
GAD1
GABAergic neurons
other neurons
Average Expression
0.4
0.0
−0.4
Percent Expressed
40
60
80
F
UMAP_2
UMAP_1
GABAergic neurons
other neurons
G
GO enrichment(BP) of diff-expression genes in progenitors
ATP metabolic process
translation
protein folding
oxidative phosphorylation
purine nucleoside diphosphate metabolic process
down−regulatd genes
regulation of proteolysis
regulation of translation
ribonucleoprotein complex biogenesis
mitochondrion organization
regulation of cellular response to stress
oxidative phosphorylation
ATP metabolic process
cytoplasmic translation
glial cell differentiation
protein localization to membrane
up−regulated genes
regulation of proteolysis
response to oxidative stress
microtubule−based movement
learning
proton transmembrane transport
−log(adjusted p value)
GO enrichment(BP) of diff-expression genes in other neurons
ATP metabolic process
oxidative phosphorylation
purine ribonucleotide metabolic process
ribonucleotide metabolic process
electron transport coupled proton transport
down−regulatd genes
response to cold
response to temperature stimulus
pyruvate metabolic process
protein folding
positive regulation of ATP biosynthetic process
cytoplasmic translation
translation
oxidative phosphorylation
ATP metabolic process
ribonucleoprotein complex biogenesis
up−regulated genes
ribosome biogenesis
ribosomal small subunit biogenesis
negative regulation of protein ubiquitination
regulation of proteolysis
regulation of translation
−log(adjusted p value)
GO enrichment(BP) of diff-expression genes in astrocytes
ATP metabolic process
oxidative phosphorylation
supramolecular fiber organization
regulation of proteolysis
down−regulatd genes
protein folding
cellular component morphogenesis
head development
response to oxygen levels
aging
positive regulation of DNA metabolic process
cytoplasmic translation
peptide biosynthetic process
ATP metabolic process
electron transport chain
ribosome biogenesis
up−regulated genes
rRNA processing
ribonucleotide biosynthetic process
mitochondrion organization
proton transmembrane transport
negative regulation of protein ubiquitination
−log(adjusted p value)
GO enrichment(BP) of diff-expression genes in oligodendrocytes
ATP metabolic process
protein folding
aerobic respiration
cellular respiration
down−regulatd genes
proton transmembrane transport
purine ribonucleotide metabolic process
nucleotide metabolic process
regulation of growth
axon extension
positive regulation of ATP biosynthetic process
cytoplasmic translation
peptide metabolic process
amide biosynthetic process
cellular amide metabolic process
oxidative phosphorylation
up−regulated genes
cellular respiration
ATP metabolic process
energy derivation by oxidation of organic compounds
glial cell differentiation
ribosomal small subunit biogenesis
−log(adjusted p value)

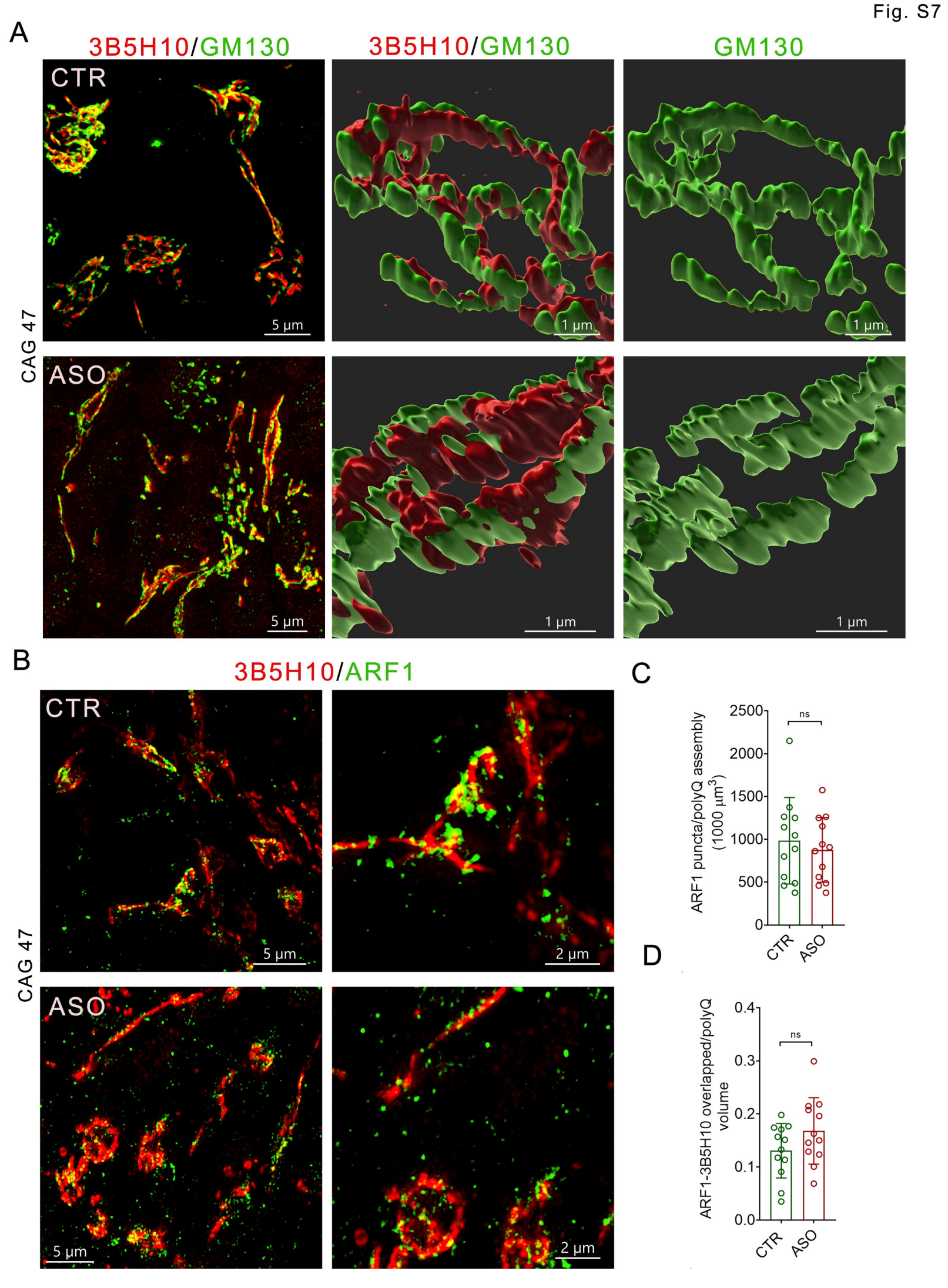
A
3B5H10/GM130
3B5H10/GM130
GM130
CAG 47
CTR
ASO
5 μm
1 μm
B
3B5H10/ARF1
2 μm
C
ARF1 puncta/polyQ assembly (1000 μm3)
ns
CTR
ASO
D
ARF1-3B5H10 overlapped/polyQ volume

Extended Data

Extended Figure legends

Figure S1. Characterization of polyQ assemblies and Golgi activities

A. LSB11011 (C-terminal of HTT) and 3B5H10 (N-terminal) antibody and phalloidin immunostaining revealed that actin filaments are enriched on the edge of large polyQ assemblies (i) or some small polyQ assembly near the cellular membrane (ii) (the boxed region indicated the sectional view in the right panel; white arrows, the polyQ assemblies interact with actin; the inner panels in ii are the spliced channels; white arrows, the interacting patterns of polyQ with F-actin).

B, C. LSB11011 (C-terminal of HTT) and 3B5H10 (N-terminal) antibodies, and phalloidin immunostaining revealed a linear assembly of polyQ on the ruffling membrane. The right panel shows a 3D image (B) revealing the alignment pattern of polyQ on membrane curvature and ruffling membrane. The image of sectional views (C) revealed the interaction pattern of polyQ with actin filaments.

D. Image sequences of the Golgi in the fibroblasts of the HD family under oxidative stress at the indicated time points.

E. The fragmentation ratio of the Golgi under H2O2 stimulation at different time points. Fragmentation ratio = number of Golgi of one cell at each time point/ number of Golgi at 0 min. Two-way ANOVA. *<0.05; **<0.01.D

F. The images of 3B5H10 and GM130 antibody immunostaining in the fibroblasts after 48 h glucose starvation, taken by SIM microscopy. The 3D-rendered tomography showed the spatial relationship between polyQ assemblies/puncta and the Golgi. The boxed regions are the magnified part or rendered region.

G, H. The changes of Golgi fragments after 48 h glucose starvation in the fibroblasts of healthy siblings (two siblings, CAG 19) and HD patients (CAG 55 and CAG 49). HD/healthy ctr, the fibroblasts cultured in high glucose medium;

HD/healthy starvation, the fibroblasts cultured in low glucose medium for 48h. Two-way ANOVA; **0.01. Cell count in each group: n>120.

I. The changes of GM130-stained Golgi sizes after 48 h glucose starvation in the fibroblasts of healthy siblings (two, CAG 19) and HD patients (CAG 55 and CAG 49). HD/healthy ctrl, the fibroblasts cultured in high glucose medium; HD/healthy starvation, the fibroblasts cultured in low glucose medium for 48h. One-way ANOVA; **0.01. The number of images in the cell line: n>20. Cell count in each group: n>400.

Figure 2. Characteristics of polyQ assembly and polyQ nuclear deposition in neurons

A. DIC images and 3D rendered tomography showing longer polyQ assemblies form a gorge in the cytoplasm or nuclear surface of induced neurons cultured for 75 days (CAG 59 and CAG 19) (pink arrow [i, ii], the gorges; white arrow, nuclear surface dents visualized by IMARIS surface). Inner panels and 3D rendered tomography displayed the spatial relationships.

B. PolyQ deposits into the nucleus and pokes the nuclear membrane of striatal neurons (white arrow, the morphology of the nucleus; yellow arrows, nucleus poked by polyQ assemblies). The lower left in right panel is an apoptotic cell (CAG, 55).

C. PolyQ precipitates occupied the nucleus of GABAergic neurons cultured for 178 days (CAG, 47).

D, E. HD patient striatal neurons derived from iPSCs cultured for 90 days (2D culture) (CAG 59) and 98 days (CAG 55) and 110 days (CAG 47) have spliced nucleus (white arrows, spliced nucleus). The summary table of nuclear splicing.

Figure 3. PolyQ assemblies in human fetal and child brains and human brain organoids with necrotic cells

A. Typical appearance of intact and continuous polyQ assemblies in the neurons of hStrO.

B. PolyQ assemblies stained by 3B5H10 antibody in fresh surgical brain tissues collected from a 4-year-old glioblastoma patient. Three representative appearances of polyQ assemblies in human brain cells. The middle panel (image-i) is a sectional view that shows a ring-like structure; the left corner insert in image-ii is a larger view; the rendered tomography shows the nuclear surface.

C.3B5H10 and ZO-1 antibodies immunostained intact polyQ assemblies in the pseudostratified neuroepithelium of the neural tube in the human fetal brain at 7.5 gestation weeks, and hCOs from HD patients, H9, and healthy siblings showed that the polyQ assemblies in the neuroepithelial cells are intact and long and formed by a small ring-like unit, and paralleled the apical-basal axis of cells.

D. Fragmented/discontinuous polyQ assemblies in freshly surged human brain samples from cortex (tissues from 4-year-old and 2-year-old glioblastoma patients).

E. The fragmentation of polyQ assemblies depends on the necrotic cells in the surrounding regions (green arrows, necrotic cells).

Figure S4. The impaired nuclear activities in HD striatal organoids

A. The validation of hCO and hStrOs by immunostaining with GSH2/MASH1 or DARPP321/CTIP2 antibodies.

B. GO analysis of differentially expressed proteins in HD striatal neurons derived from iPSCs and healthy GABAergic neurons derived from iPSCs at 60 100 days (CAG 55 vs. H9 and CAG 19).

C. The validation of hCO by immunostaining with PAX6/TBR2 /HOPX or TBR1/CTIP2/SATB2 antibodies.

Figure 5. ARF1 levels were reduced in HD neurons

A. The immunostaining results of ARF1, CTIP2, and 3B5H10 antibodies in the neurons of hStrOs (CAG 49 and CAG 19). The middle panels showed ARF1 signals.

B, C. The overlapped volume of ARF1 with polyQ in the HD and healthy

neurons of hStrOs (G). The ratio of ARF1 volume/polyQ volume in CTIP2 + regions. The surface function of IMARIS was used to calibrate volume. Object-object statistics in IMARIS measure the overlapped volume. t-test, *<0.05; **<0.01..

D. The immunostaining results of ARF1, CTIP2, and GM130 antibodies in the neurons of hStrOs (CAG 49 and CAG 19). The middle panels showed ARF1 signals.

E, F. The overlapped volume of ARF1 with the Golgi in the HD and healthy neurons of hStrOs. The ratio of ARF1 volume/Golgi volume in CTIP2 + regions. The surface function of IMARIS was used to calibrate volume. Object-object statistics in IMARIS measure the overlapped volume. t-test, **, p<0.01.

G. Bulk RNAseq data of HD hStrOs (CAG 55 and 59) and healthy hStrOs (CAG 19 and H9) at 60 days revealed *ARF1* transcription levels. *Student t-test; *<0.05; **<0.01.*

H. The bulk RNAseq data of HD hStrOs (CAG 55 and 59) and healthy hStrOs (CAG 19 and H9) at 80 days revealed *ARF1.* Student t-test; ***, p<0.01.* CTR, healthy.

Figure S6. Characterizing and sorting the cellular types from scRNA-seq data of hStrOs and GO analyses of different cellular clusters in scRNA-seq data of hStrOs

A. Expression of known markers of progenitor, neuron, astrocyte and oligodendrocyte.

B. Stacked bar plots and a pie chart representing the proportion of cell types.

C, D. Expression of known markers of LGE progenitors and cortical progenitors(C), GABAergic neurons and glutamatergic neurons (D).

E. Dot plot displaying expression of GABAergic neurons marker genes.

F. UMAP plot of neurons colored by GABAergic neurons (red) and other neurons (grey).

G. GO enrichment analysis of down-regulated (top) and up-regulated (bottom)

genes in CAG59 VS CAG19/H9 progenitor, other neuron, astrocyte, and oligodendrocyte.

Figure 7. ASO treatments did not alter Golgi morgphology and ARF1 scaffolding in polyQ assembly

A. The representative super-resolution images of polyQ assemblies stained by 3B5H10 antibody and Golgi stained by GM130 antibody in ASO-treated and control h hCOs. The middle and right panels show the spatial relationships between polyQ assemblies and the Golgi, and the tomography of the Golgi, respectively. The renderings are done by IMARIS surface.

B. The representative super-resolution images of polyQ assemblies stained by 3B5H10 antibody and ARF1 puncta in ASO-treated and control (CTR) hCOs. The images are displayed as MIP. The rights are the magnified region in the rectangle on the left.

C. The density of ARF1+ puncta in polyQ assemblies ASO-treated and control (CTR) hCOs (HD, n=2 [CAG 47 and CAG 59]; hCOs, n=6; t-test, ns>0.05). Puncta are counted with the IMARIS surface.

D. The overlapped volume of ARF1 puncta with polyQ assemblies in ASO-treated and control (CTR) hCOs. (HD, n=2 [CAG 47 and CAG 59]; hCOs, n=6; t-test, ns>0.05). polyQ assembly and puncta volume are measured by the IMARIS surface.

Supplementary Materials and Methods

Supplementary Materials and Methods

Primer and sequencing

A nurse collected blood from the upper arm vein, and a Blood DNA Isolation Kit extracted blood DNA. After PCR amplification, the mutant band separates from the wild-type band on a 4% Agarose gel, and the band is then cut and extracted using a DNA Gel Extraction Kit (GenElute™, Sigma-Aldrich). The extract was sequenced by the Sanger method.

The sequencing primers:

A1: 5'-CAGAGCCCCATTCATTGCC-3'

B1: 5'-TGAGGAAGCTGAGGAGGC-3'

Glucose starvation assays for polyQ assemblies and Golgi

Cultured the fibroblasts in a 24-well plate with cover glasses (Φ20mm). After two days, the medium was replaced by low-glucose medium without FBS. The cells in low-glucose medium were fixed at 24 h, 48 h, and 72 h, and stained with the 3B5H10 antibody and phalloidin. At 72 h, the medium was replaced with high-glucose medium lacking FBS and cultured for an additional 48 h, then fixed and stained with 3B5H10 antibody and phalloidin. ImageJ software was used to measure the polyQ assemblies. Imaris was used to render the image. A group of fibroblasts was stained by GM130 antibodies at 48 h after supplying low-glucose medium for Golgi changes.

Onjisaponin and ASO treatments

The sequence of HuASO: 5’-CTCAGtaacattgacACCAC-3'. 5mg HuASO were synthesized by WuXi AppTec. ASOs were solubilized in 0.9% sterile saline solution or PBS. Onjisaponin F was purchased from Jindu Biotech of Shanghai and dissolved in DMSO to a concentration of 100 mM.

Brain organoids (day 100) were treated continuously for 10 days with ASOs at final concentrations of 40 μg/mL. And fibroblasts were treated continuously for 5 days with ASOs at final concentrations of 20, 40 μg/mL. Vehicle (PBS) were used as controls. ASOs were solubilized in sterile PBS and

supplemented directly into the culture medium, with media and ASO replenishment every 24 hours.

Immunostaining

Cells, tissues, or organoids were fixed in fresh ice-cold 4% PFA for 15-30 minutes and overnight, respectively. After fixation, immunostaining was performed as previously described[1]. Primary antibodies were used as follows: anti-Tuj-1 antibodies (mouse, Sigma, T8860 , 1:5000; rabbit, Covance Research Products, PRB-435P, 1:5000), 3BH10 antibody (Mouse，Sigma, P1874，1:10000), anti GABA antibodies (rabbit, Sigma, A2052, 1:5000; mouse; Sigma, A0310，1:500), Clathrin antibody (Rabbit, Abcam, ab21679, 1:1000), GM130 antibody (Rabbit, Abcam, ab52649, 1:1000), IHC‑plus™ Polyclonal Rabbit anti‑Human HTT / Huntingtin Antibody (C‑Terminus, LS-B11011, 1:200). Secondary antibodies used were as follows: Alexa Fluro 488 Donkey anti-mouse IgG (Invitrogen, Molecular Probe, A21202, 1:1000), Alexa Fluro 594 Donkey anti-mouse IgG (Invitrogen, Molecular Probe, A21203,1:1000), Alexa Fluro 594 Donkey anti-rabbit IgG(Chemicon, A21207,1:1000), Alexa Fluro 488 Donkey anti-rabbit IgG (Invitrogen, Molecular Probe, A21206,1:1000), Alexa Fluro 594 Donkey anti-goat IgG (Invitrogen, Molecular Probe, A11058,1:1000) Cy5 AffiniPure Donkey Anti-Goat IgG (H+L) (Jackson, 705-175-147,1:300), Cy5 AffiniPure Donkey Anti-Rabbit IgG (H+L) (Jackson, 711-175-152,1:300), Alexa Fluo 633 Phalloidin (Invitrogen, A22284,1:200), Mito-Tracker™ Green (Invitrogen, M7514), ER-Tracker™ Green (Invitrogen, E34251), DAPI (Sigma, D9542), Phalloidin Alexa-633 or 488 (ThermoFisher, A12379 or A22284, 1:1000), GOLGI ID® Green assay kit (ENZO, ENZ-51028-K100).

Golgi apparatus-selective staining and imaging in live cells

Replated fibroblasts in glass-bottomed 35mm dishes (biosharp, BS-20-GJM). The Golgi apparatus in live cells was labeled with the GOLGI ID Green assay kit (ENZO, ENZ-51028-K100), a Golgi-selective dye. The Assay Solution and

the Detection Reagent according to the manufacturer's guidelines. After preparation, these agents were fully mixed. After washing the cells with Assay Solution, a sufficient volume of Detection Reagent was dispensed to cover the monolayer cells, and the cells were incubated for 30 minutes at 37°C. Before imaging, the cells were washed 3 times and incubated in medium at 37°C for another 30 minutes. For imaging, sequential images were captured from multiple ROIs (regions of interest) in dishes. The time intervals were 30 min, 60 min, 120 min, and 240 min.

2D Neural differentiation

The cells were differentiated according to the neural differentiation protocol described [1]. Briefly, dissociated WT-iPS and HD-iPS cells were plated on Matrigel (BD) at a density of 3.5×104 cells/cm2 and maintained in E8 medium (Thermo Fisher Scientific) for 4-5 days until they reached 90% confluence. After digestion with EDTA, 9000 cells were plated in each well of U-shaped 96-well plates (SUNILON). On the first day, we maintained these cells in E8 and hNM (1:1 mixture). On the second day, the medium was replaced with hNM. From day 0 to day 6, the medium containing 2 μMol/L SB431542 (Tocris) and 0.3 μMol/L LDN193189 (BMP inhibitor, Tocris) was used for culture. These cells were plated in a well on day 7, and 200 ng/ml SHH or 0.65 μM Purmorphamine was supplied on day 10 for the differentiation of GABAergic neurons. The cells were maintained in the same medium for 2 weeks. The medium without SHH or Purmorphamine is used for differentiating glutamate neurons. At 15 days of differentiation, the rosettes were collected and cultured in a suspension condition for 25 days. On day 25, these cells were plated on a cover glass double-coated by polyonithin and laminin after digesting with accutase and then supplemented by a neural induction medium (composed of Neurobasal, N2 100×, B27 50×) (Invitrogen), supplemented with 10 ng/ml BDNF (Peprotech), 10 ng/ml GDNF (Peprotech) and 10 ng/ml IGF (Peprotech).

Human brain organoid construction

Brain organoids were constructed according to our protocol 2. Briefly, ES/iPS colonies were dissociated into single cells using Accutase (Gibco, A1110501). 9,000 dissociated cells were plated into each well of a V-bottom ultra-low-attachment 96-well plate (Sumitomo Bakelite, MS-9096VZ). Induction media contained Human Neural differentiation Medium and E8 media (1:1), supplemented with the two SMAD inhibitors 0.3μM LDN-193189 (STEMGENT, 040074), 2μM SB431542 (Ametek Scientific, DM-0970), and 10 μm Y-27632 (APE.BIO, A3008). On the sixth day in suspension, hCOs were transferred to neural differentiation media containing a 1:1 mixture of DMEM-F12 media and Neurobasal media supplemented with 1% (v/v) MEM-NEAA (Gibco, 11140-050), 1% (v/v) GlutaMAX(Gibco, 35050-061), 1% (v/v) N2 supplement (Gibco, 17502-048), 2% (v/v) B27 supplement (Gibco), 1% (v/v) Penicillin/Streptomycin (Gibco, 2051357). Growth factors 10ng/ml EGF (R&D Systems, 236-EG) and 20 ng/ml bFGF (R&D Systems, 233FB/CF) were used from day6 to day23. Growth factors, the 20 ng/ml BDNF (Peprotech, AF450002) and 10 ng/ml GDNF (Peprotech, AF450010) were used from day 24 to day 45.

Interfacing the brain organoid with HD-MEA

To facilitate robust hCO-electrode coupling, high-density microelectrode array (HD-MEA) chips (Maxlab Biosystems, Switzerland) were first functionalized. The sensing area was treated with a 0.07% (v/v) poly(ethylenimine) (PEI; Sigma-Aldrich) solution followed by a coating of laminin. For the interfacing of hCOs, we adapted the manufacturer's protocols for brain slices. Individual hCOs were meticulously transferred to the center of the coated electrode arrays. To ensure mechanical stability and intimate contact between the basal surface of the organoid and the electrodes, a small droplet of Matrigel (Corning) was applied to secure the tissue. The chips were then lidded and incubated at 37 °C with 5% CO_2 for 30 minutes to allow for matrix gelation. Subsequently, the culture was replenished with BrainPhys neuronal medium (StemCell Technologies) supplemented with the following

reagents: 2% (v/v) NeuroCult SM1 Neuronal Supplement (StemCell Technologies), 1% (v/v) N2 Supplement-A (Gibco), 1x GlutaMAX (Gibco), 20 ng/ml recombinant human BDNF, 20 ng/ml recombinant human GDNF (PeproTech), 20 ng/ml NT-3 (PeproTech), 1 mM dibutyryl-cAMP (Sigma-Aldrich), and 1x Antibiotic-Antimycotic (Gibco). The recording medium was changed every 2–3 days.

Electrophysiological recordings

To probe network activity in hCOs, longitudinal HD-MEA recordings were used. The spontaneous activity was recorded sequentially in blocks across the entire array (30 seconds per recording configuration, each comprising 1020 recording electrodes). Signals were sampled at 20 kHz for all recordings and saved in an HDF5 file format. Spike detection was performed using a threshold set to 5× the root-mean-square (RMS) of the noise in the band-pass-filtered signal. After the activity scan, the readout electrodes were selected depending on the requirements of each analysis (single-cell or network-related features). All HD-MEA recordings of hCOs started at least 7 days after plating. The reported electrophysiological results are based on data obtained from n=3 hCOs (CTR group), n=3 hCOs (HD group), and n=3 hCOs (HD group with ASO treatment).

Preparation and data analysis of a single-cell RNA-sequencing library

110 days differentiated hStrOs from a HD patient (CAG 59), a healthy sibling, and H9 in suspension culture are prepared for analysis. A sterile dish with 10 ml 1x Dulbecco's Phosphate-Buffered Saline (DPBS; Thermo Fisher, 14190144) on ice is used to transport samples after removing the residual solution. Neurosphere Dissociation Kit (Miltenyi, 130-095-943) used to create single-cell suspensions. Dissociated cells were rinsed 1x DPBS containing 2% FBS. 0.4% Trypan blue staining (Thermo Fisher, 14190144) is used to assess viability on the Countess® II Automated Cell Counter (Thermo Fisher).

10x library preparation and sequencing

Beads with unique molecular identifier (UMI) and cell barcodes were

loaded close to saturation, so that each cell was paired with a bead in a Gel Beads-in-emulsion (GEM). After exposure to cell lysis buffer, polyadenylated RNA molecules hybridized to the beads. Beads were retrieved into a single tube for reverse transcription. For cDNA synthesis, each cDNA molecule was tagged at the 5' end (i.e., the 3' end of a messenger RNA transcript) with a UMI and a cell label indicating its cell of origin. Briefly, 10× beads that were then subject to second-strand cDNA synthesis, adaptor ligation, and universal amplification. Sequencing libraries were prepared from randomly interrupted whole-transcriptome amplification products to enrich for the 3' ends of transcripts linked to the cell barcode and UMI. All remaining procedures, including library construction, were performed according to the manufacturer's standard protocol (Chromium Single Cell 3' v3). A High Sensitivity DNA Chip (Agilent) on a Bioanalyzer 2100 and the Qubit High Sensitivity DNA Assay (Thermo Fisher Scientific) quantified NovaSeq6000 (Illumina) sequencing libraries (2x150 chemistry).

Single cell RNA-seq data processing and analysis

Cell Ranger 4.0 pipeline with default and recommended parameters processed the reads. Gene-Barcode matrices were generated for each sample by counting UMIs and filtering out non-cell-associated barcodes, and a gene-barcode matrix containing the barcoded cells and gene expression counts was generated. After obtaining the single-cell expression matrix, we used the Seurat (v4.0.5)[2] R toolkit to perform normalization, clustering, dimensionality reduction, and visualization. Cells that had the number of detected genes less than 200 and the percentage of mitochondrial genes lower than 10% were removed. Gene counts were then log-transformed and scaled, and 3000 shared highly variable genes were identified using the FindVariableFeature function. We applied the Runharmony function with the Seurat-based principal component analysis (PCA) reduction method in the Harmony (v0.1.0)[3] package to correct batch effects and generate low-dimensional matrices. A nearest-neighbor graph was calculated using

FindNeighbors and clustered using FindClusters, followed by visualization of the cell clusters using uniform manifold approximation and projection (UMAP). We used the well-known marker genes to assign these clusters to corresponding cell types. Differentially expressed genes(|log2FC|>0.25 and adjusted p value<0.01) among GABAergic neurons (CAG 59 vs CAG 19, CAG 59 vs H9) were identified by the Seurat function FindMarkers.

Functional enrichment

Enrichment GO categories for significantly differentially expressed genes were identified by Metascape (https://metascape.org/gp/)[4], which utilizes hypergeometric test and Benjamini-Hochberg p-value correction algorithm to identify acceptable ontology terms. Adjusted p value of GO biological processes <0.01 was considered to be significant enrichment terms. The gene set enrichment score of Golgi vesicle transport (GO:0048193) was calculated by AUCell(v.1.14.0)[5]. The AUCell_buildRankings and AUCell_calcAUC algorithms were used for ranking model building and calculating "Area Under the Curve" (AUC) scores.

LC-MS analysis

The patients' iPSCs were differentiated for 50 or 100 days, and the samples were then sent to the core facility of the State Key Laboratory of Genetic Engineering for analysis. The FASP digestion was adapted for the following procedures in Microcon PL-10 filters. After a three-time buffer displacement with 8 M Urea and 50 mM ABC, pH 8.5, proteins were reduced by 10 mM DTT at 37 °C for 30 min, followed by alkylation with 30 mM iodoacetamide at 25 °C for 45 min in a light-proof condition. Digestion was performed with trypsin (enzyme/protein ratio 1:50) at 37 °C for 12 h, after which the sample was rinsed with 20% ACN and buffer displaced three times with digestion buffer (10 mM ABC). After digestion, the solution was filtered, the filter rinsed twice with 15% ACN, and the filtrates were pooled and vacuum-dried. LC-MS analysis was performed using a nanoflow EASYnLC 1200 system (Thermo Fisher

Scientific, Odense, Denmark) coupled to an Orbitrap Exploris 480 mass spectrometer (Thermo Fisher Scientific, Bremen, Germany). A one-column system was adopted for all analyses. A home-made C18 analytical column (75 μm i.d. × 25 cm, ReproSil-Pur 120 C18-AQ, 1.9 μm (Dr. Maisch GmbH, Germany) was used to analyze samples. The mobile phases are composed of Solution A (0.1% formic acid) and Solution B (0.1% formic acid in 80%ACN). The derivatized peptides were eluted using the following gradients: 5–8% B in 2 min, 8–44% B in 98 min, 44–60% B in 3 min, 60–100% B in 2 min, 100% B for 10 min, at a flow rate of 200 nL min. High-field asymmetric-waveform ion mobility spectrometry (FAIMS) was enabled during data acquisition, with compensation voltages set to −45 and −65 V. MS1 data were collected in the Orbitrap (60,000 resolution). Charge states 2-7 were required for MS2 analysis, and a 45 s dynamic exclusion window was used. Cycle time was set at 1.5 s. MS2 scans were performed in the Orbitrap with HCD fragmentation (isolation window 1.6; 15,000 resolution; NCE 30%).

Data availability

The sequencing datasets generated and/or analyzed during this study are available in the Sequence Read Archive (SRA) and Gene Expression Omnibus (GEO) with the following accession numbers for anyone: Day 60 and Day 80 MSN in hStrO for bulk RNA-seq (PRJNA760260), Day 110 MSN culture in hStrO for scRNA-seq (GSE184255). The proteomic data are available to anyone for reasonable requests.

Reference

1 Ma, L. *et al.* Human embryonic stem cell-derived GABA neurons correct locomotion deficits in quinolinic acid-lesioned mice. *Cell Stem Cell* **10**, 455-464, doi:10.1016/j.stem.2012.01.021 (2012).

2 Butler, A., Hoffman, P., Smibert, P., Papalexi, E. & Satija, R. Integrating single-cell transcriptomic data across different conditions, technologies, and species. *Nature Biotechnology* **36**, 411-+, doi:10.1038/nbt.4096 (2018).

3 Korsunsky, I. *et al.* Fast, sensitive and accurate integration of single-cell data with Harmony. *Nature Methods* **16**, 1289-+, doi:10.1038/s41592-019-0619-0 (2019).

4 Zhou, Y. Y. *et al.* Metascape provides a biologist-oriented resource for the analysis of systems-level datasets. *Nat Commun* **10**, doi:ARTN 1523
10.1038/s41467-019-09234-6 (2019).

5 van de Sande, B. *et al.* A scalable SCENIC workflow for single-cell gene regulatory network analysis. *Nature Protocols* **15**, 2247-2276, doi:10.1038/s41596-020-0336-2 (2020).